MOLECULAR BIOLOGY

Optineurin regulates NRF2-mediated antioxidant response in a mouse model of Paget's disease of bone

Xiangxiang Hu[1,2,3], Sing-Wai Wong[4,5], Kaixin Liang[1,6,7], Tai-Hsien Wu[3], Sheng Wang[3], Lufei Wang[1,8], Jie Liu[3], Mitsuo Yamauchi[2], Brian L. Foster[9], Jenny P.-Y. Ting[6,7,10], Baohong Zhao[11,12,13], Henry C. Tseng[14], Ching-Chang Ko[3]*

Degenerative diseases affecting the nervous and skeletal systems affect the health of millions of elderly people. Optineurin (OPTN) has been associated with numerous neurodegenerative diseases and Paget's disease of bone (PDB), a degenerative bone disease initiated by hyperactive osteoclastogenesis. In this study, we found age-related increase in OPTN and nuclear factor E2-related factor 2 (NRF2) in vivo. At the molecular level, OPTN could directly interact with both NRF2 and its negative regulator Kelch-like ECH-associated protein 1 (KEAP1) for up-regulating antioxidant response. At the cellular level, deletion of OPTN resulted in increased intracellular reactive oxygen species and increased osteoclastogenic potential. At the tissue level, deletion of OPTN resulted in substantially increased oxidative stress derived from leukocytes that further stimulate osteoclastogenesis. Last, curcumin attenuated hyperactive osteoclastogenesis induced by OPTN deficiency in aged mice. Collectively, our findings reveal an OPTN-NRF2 axis maintaining bone homeostasis and suggest that antioxidants have therapeutic potential for PDB.

INTRODUCTION

Age-dependent tissue degeneration leads to many diseases that negatively affect the health and quality of life of elderly people (*1*, *2*). Along with the nervous system, bones are among the most vulnerable organs to degenerate (*3*, *4*). Recently, optineurin (OPTN), a multifunctional protein previously associated with numerous neurodegenerative diseases, was genetically implicated in Paget's disease of bone (PDB) (*5*–*7*). In PDB, a pathological increase in cells that degrade bone (called osteoclasts) leads to abnormal bone remodeling (*8*). Affected individuals suffer debilitating bone fractures, poor healing, neuropathic pain, and increased mortality (*9*). The cause of PDB is unknown. There are no cures and treatment options are limited (*10*). The genetic association of OPTN with neurodegeneration and PDB suggests a role in maintaining cellular homeostasis, but its function remains poorly understood.

To study OPTN's function in cellular degeneration and specifically in PDB, we previously reported the development and characterization of a mouse model based on the ubiquitous deletion of OPTN ($Optn^{-/-}$, $-/-$). These mice recapitulate key phenotypic features of PDB clinical and histological findings, compared to their wild-type ($Optn^{+/+}$, $+/+$) littermates (*11*). Our subsequent in vitro studies revealed that loss of OPTN altered nuclear factor E2-related factor 2 (NRF2) expression during osteoclastogenesis. This, in turn, modulated cellular antioxidant responses to reactive oxygen species (ROS) (*12*). This OPTN-NRF2 signaling axis regulation of ROS levels had not been previously reported. Loss of OPTN and increased ROS levels were found to stimulate in vitro formation of osteoclasts (called osteoclastogenesis) and osteoclast function (*12*). However, at the in vivo level, it remains unclear whether collective changes in OPTN, NRF2, and ROS levels are actually responsible for clinical findings of bone loss and abnormal remodeling in PDB.

Because tissue levels of ROS are largely generated by mitochondrial respiratory activity, highly metabolically active cells such as osteoclasts generate high levels of ROS (*13*, *14*). ROS has been reported to function as an intracellular signal mediator of osteoclastogenesis and, thus, can trigger bone turnover (*15*, *16*). However, excessive intracellular ROS exerts oxidative stress resulting in biochemical and structural damage. Among various tissue environmental factors, oxidative stress has also been associated with neurodegeneration and abnormal bone remodeling in vivo (*17*–*19*). Although several classic molecular pathways have been implied (*20*–*22*), how ROS homeostasis is maintained and regulated in bone largely remains unknown.

ROS levels are indirectly regulated by the NRF2-antioxidant system, which neutralizes excessive ROS to avoid accumulation and tissue damage (*23*). At basal levels, NRF2 is bound to its negative regulator, Kelch-like ECH-associated protein 1 (KEAP1), which results in rapid NRF2 turnover and degradation in the cytoplasm.

[1]Oral and Craniofacial Biomedicine Program, Adams School of Dentistry, University of North Carolina at Chapel Hill, Chapel Hill, NC 27599, USA. [2]Division of Oral and Craniofacial Health Sciences, Adams School of Dentistry, University of North Carolina at Chapel Hill, Chapel Hill, NC 27599, USA. [3]Division of Orthodontics, The Ohio State University College of Dentistry, Columbus, OH 43210, USA. [4]Division of Comprehensive Oral Health, Adams School of Dentistry, University of North Carolina at Chapel Hill, Chapel Hill, NC 27599, USA. [5]Stomatology Hospital, School of Stomatology, Zhejiang University School of Medicine, Zhejiang Provincial Clinical Research Center for Oral Diseases, Key Laboratory of Oral Biomedical Research of Zhejiang Province, Hangzhou 310006, China. [6]Lineberger Comprehensive Cancer Center, University of North Carolina at Chapel Hill, Chapel Hill, NC 27514, USA. [7]Department of Genetics, University of North Carolina at Chapel Hill, Chapel Hill, NC 27514, USA. [8]Guangxi Key Laboratory of the Rehabilitation and Reconstruction for Oral and Maxillofacial Research; Department of Orthodontics, College and Hospital of Stomatology, Guangxi Medical University; Nanning, Guangxi 530021, China. [9]Division of Biosciences, The Ohio State University College of Dentistry, Columbus, OH 43210, USA. [10]Department of Microbiology and Immunology, University of North Carolina at Chapel Hill, Chapel Hill, NC 27514, USA. [11]Arthritis and Tissue Degeneration Program and David Z. Rosensweig Genomics Research Center, Hospital for Special Surgery, New York, NY 10021, USA. [12]Department of Medicine, Weill Cornell Medical College, Cornell University, New York, NY 10065, USA. [13]Graduate Program in Cell and Development Biology, Weill Cornell Graduate School of Medical Sciences, New York, NY 10065, USA. [14]Duke Eye Center and Department of Ophthalmology, Duke University Medical Center, Durham, NC 27710, USA.
*Corresponding author. Email: ko.367@osu.edu

With increased ROS, KEAP1 dissociates and allows NRF2 to enter the nucleus and enhance the expression of downstream antioxidants, which, in turn, quenches ROS (*24*, *25*). Our previous work demonstrated that OPTN and NRF2 directly interact through specific binding sites. Moreover, we found that a deficiency of OPTN resulted in compromised NRF2-induced antioxidant response in osteoclasts (*12*). However, it remains unknown how OPTN interacts with NRF2 in vivo in actual bone tissue, how the interaction changes with age, and how these changes contribute to tissue degeneration.

In this study, we test the hypothesis that compromised Nrf2-induced antioxidant response leads to age-dependent degeneration in OPTN-associated bone loss. We demonstrate that age-dependent changes in OPTN-NRF2 axis play a critical role in PDB pathophysiology. We also provide evidence that restoration of NRF2 antioxidant response minimizes age-dependent OPTN-mediated bone loss. This constitutes a possible therapeutic strategy for treating oxidative stress and PDB. This work improves our understanding of the pathogenesis of OPTN-associated PDB and possibly other OPTN-associated neurodegenerative diseases.

RESULTS

OPTN expression increases with age and is highly colocalized with NRF2 in the bone

It is not clear how OPTN expression changes with age in the bone and whether OPTN interacts with NRF2 in vivo. Therefore, we examined the expression of NRF2 and OPTN in young and aged wild-type (*Optn$^{+/+}$*) mice. Western blotting of whole bone marrow lysates showed significantly higher levels of both NRF2 and OPTN in aged versus young bones (Fig. 1A). This is in contrast to young bones that expressed very low levels of NRF2 and OPTN. Quantitation of the bands showed that bones from older mice expressed sixfold higher levels of NRF2 ($P < 0.001$) and eightfold higher of OPTN ($P < 0.001$) than young mice (Fig. 1B).

These findings were confirmed by confocal microscopy of immunofluorescent bone staining. First, marked increase in OPTN within the bone marrow was observed with increasing age (Fig. 1, C and D). Confocal images revealed that OPTN and NRF2 were highly colocalized regardless of age, but their intensity and distributions changed markedly over time. Notably, some hollow, nodular areas (shown by the arrow in Fig. 1C) were highly colocalized for OPTN and NRF2 in both young and aged bones. In contrast, there were regions where OPTN-NRF2 colocalizations (shown by the triangle in Fig. 1C) were observed only in aged bones.

Next, we visualized OPTN and NRF2 separately with both tartrate-resistant acid phosphatase (TRAP; an osteoclast marker) and alkaline phosphatase (ALP; an osteoblast marker) (fig. S1, A and B) in long bones from normal young mice to determine the type of cells that were expressing OPTN and/or NRF2. Hollow, nodular areas (arrow with triangle head) containing TRAP-positive osteoclasts showed strong colocalization with OPTN and NRF2. In contrast, ALP areas curvilinear in shape containing osteoblasts (arrow) showed less colocalization of OPTN and NRF2. The bone marrow exhibited many tiny irregular areas (triangle) with cells that were neither TRAP nor ALP positive but were notably OPTN and NRF2 positive.

Together, our Western blotting and immunofluorescent experiments showed that both OPTN and NRF2 expression levels increase with age. Moreover, OPTN and NRF2 expression are highly colocalized to primarily osteoclasts but relatively less in osteoblasts and other bone cells. These findings also suggest that OPTN might regulate NRF2 expression as a function of age, which we investigate further in the following sections.

OPTN modulates NRF2 expression and interacts with the NRF2 regulator KEAP1

NRF2-induced antioxidant response is regulated by a protein called KEAP1 through direct protein binding (*25*). Both proteins are tightly bound until increased ROS levels induce KEAP1 to release NRF2 to initiate an antioxidant response. We hypothesized that OPTN interacts with NRF2 through KEAP1. To test this possibility, we examined the extent that OPTN, NRF2, and KEAP1 might colocalize to up-regulate NRF2-induced antioxidant response. Osteoclasts from *Optn$^{-/-}$* mice, *Optn$^{+/+}$* mice, and the *Optn$^{+/+}$* cells after OPTN overexpression were compared for NRF2 nuclear translocation, as well as for OPTN, NRF2, and KEAP1 colocalization. Western blotting of cytoplasmic and nuclear extractions showed that the incremental expression of OPTN was restricted to cytoplasm but resulted in less NRF2 degradation in cytoplasm and more NRF2 nuclear translocation (Fig. 2, A and B), suggesting OPTN as a positive regulator in cytoplasm for NRF2-induced antioxidant response. In analyzing the colocalization, with increased nuclear 4′,6-diamidino-2-phenylindole (DAPI)–NRF2 colocalization following OPTN overexpression, we detected increased colocalization of both OPTN-NRF2 and OPTN-KEAP1 following increased OPTN expression and nuclear (DAPI)–NRF2 (Fig. 2C). These findings suggest that OPTN may up-regulate NRF2 nuclear translocation through interactions with both NRF2 and KEAP1.

We have previously shown direct binding and perinuclear colocalization between OPTN-NRF2 (*12*). To determine whether OPTN might biochemically interact with KEAP1 directly, we performed a coimmunoprecipitation (co-IP) experiment to test potential OPTN-KEAP1 binding. As expected, transient overexpression of the hemagglutinin (HA)–tagged KEAP1 and the enhanced green fluorescent protein (eGFP)–tagged OPTN was accomplished in human embryonic kidney (HEK) 293 cells. We found that eGFP-OPTN was pulled down by anti-HA antibodies (Fig. 2D). This result suggests that OPTN can bind to KEAP1 directly. We further performed endogenous co-IP to confirm the binding of OPTN-KEAP1 in osteoclasts (fig. S2A). Previous findings suggest that NRF2-KEAP1 binding is independent from OPTN and OPTN-NRF2 binding is independent from KEAP1 (*12*). To determine whether NRF2 is required for the OPTN and KEAP1 binding, we knocked down NRF2 using a small interfering RNA targeting *Nrf2* (si*Nrf2*) in preosteoclasts where KEAP1 was more prominent in cytoplasm. We then visualized OPTN, NRF2, and KEAP1 by immunostaining and confocal microscopy. By comparing the level of OPTN-KEAP1 colocalization between the si*Nrf2*-treated cells and the regular cells, we did not observe loss or significant decrease in OPTN-KEAP1 binding in the setting of NRF2 silencing (fig. S2B). The above data suggest that OPTN-KEAP1 binding is independent from NRF2 and that OPTN-NRF2 and OPTN-KEAP1 binding are important parts of the regulatory mechanism underlying the OPTN-NRF2 axis.

Next, we immunostained for OPTN, NRF2, and KEAP1 in both osteoclastic areas and nonosteoclastic areas of the bone marrow in *Optn$^{+/+}$* mice. Besides colocalization with NRF2, OPTN was found
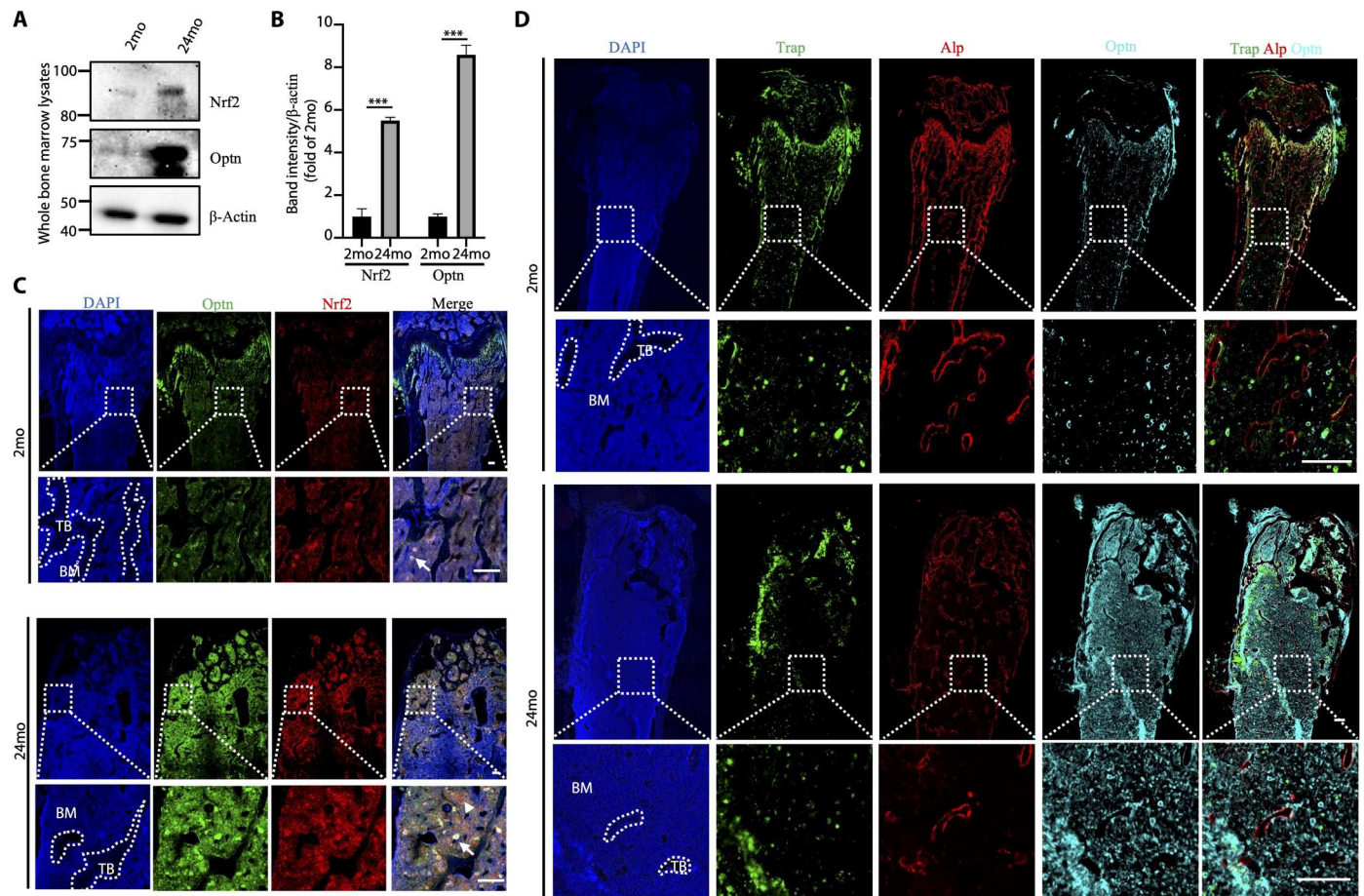
Fig. 1. OPTN expression increases with age and is highly colocalized with NRF2 in the bone. (**A**) Immunoblot analysis of femur whole bone marrow lysates for NRF2 and OPTN expression in 2-month-old (2mo) and 24-month-old (24mo) mice. β-Actin was used as control. (**B**) Quantitation of immunoblot in 2-month-old (black bars) and 24-month-old (gray bars) mice. There is a sixfold increase in NRF2 and eightfold increase in OPTN in older animals. Data presented as averages ± SEM; $n = 3$ blots; ***$P < 0.001$. (**C**)Localization of DAPI, OPTN, and NRF2. Arrow indicates osteoclasts areas, and triangle indicates areas in the bone marrow showing high OPTN/NRF2 colocalization. (**D**) Representative images showing localization of DAPI, TRAP, ALP, and OPTN in femurs. TRAP is a marker for osteoclasts, while ALP is a marker for osteoblasts. (C and D) Representative images of femur trabeculae (TB) and bone marrow (BM) in 2- and 24-month-old animals. Scale bars, 250 μm (for both low and high power views).

to be highly colocalized to KEAP1 (Fig. 2E). Osteoclastic areas identified by morphology consistently showed colocalization of OPTN-NRF2 and OPTN-KEAP1 regardless of age (Fig. 2, E and F). In contrast, nonosteoclastic areas in the bone marrow showed a switch of colocalization pattern, from predominantly NRF2-KEAP1 in young bones to a much higher level of both OPTN-NRF2 and OPTN-KEAP1 in aged bones (Fig. 2, E and F). Together, these findings on KEAP1 colocalization further support OPTN's interaction with NRF2 and role in regulating ROS and osteoclastogenesis.

Deletion of OPTN results in decreased NRF2 in aged osteoclasts and other bone marrow cells

Our previous in vitro study found that, following receptor activator of nuclear factor κampt;Beta; ligand (RANKL) induction, preosteoclasts lacking OPTN generate higher level of ROS intracellularly to further up-regulate osteoclastogenic activity and formation of osteoclasts (*12*). In addition, we also found that OPTN deficiency is associated with compromised *Nrf2*-induced antioxidant response in vitro, which normally neutralizes ROS to prevent excessive

accumulation (*12*). Therefore, we hypothesized that NRF2-induced antioxidant response would also be compromised in vivo in osteoclasts of *Optn*$^{-/-}$ mice and that this would worsen with increasing age. If this hypothesis were true, then it predicts that *Optn*$^{-/-}$ mice will demonstrate increased ROS and osteoclastogenic activity.

To test this, we visualized NRF2 in femurs from *Optn*$^{-/-}$ mice using immunofluorescent staining and confocal microscopy. These were costained for TRAP. TRAP staining was highly colocalized with NRF2 in the bones of both *Optn*$^{+/+}$ and *Optn*$^{-/-}$ mice (Fig. 3A). This colocalization pattern was observed in young and aged animals from both genotypes. However, in bones from older animals, there was significantly less NRF2 expression in *Optn*$^{-/-}$ versus *Optn*$^{+/+}$ osteoclasts. NRF2 staining intensity was lower, and there were fewer NRF2-immunopositive areas. No difference in NRF2 expression was observed in bones from young animals when comparing *Optn*$^{+/+}$ and *Optn*$^{-/-}$ mice. This is quantitatively shown in Fig. 3C.
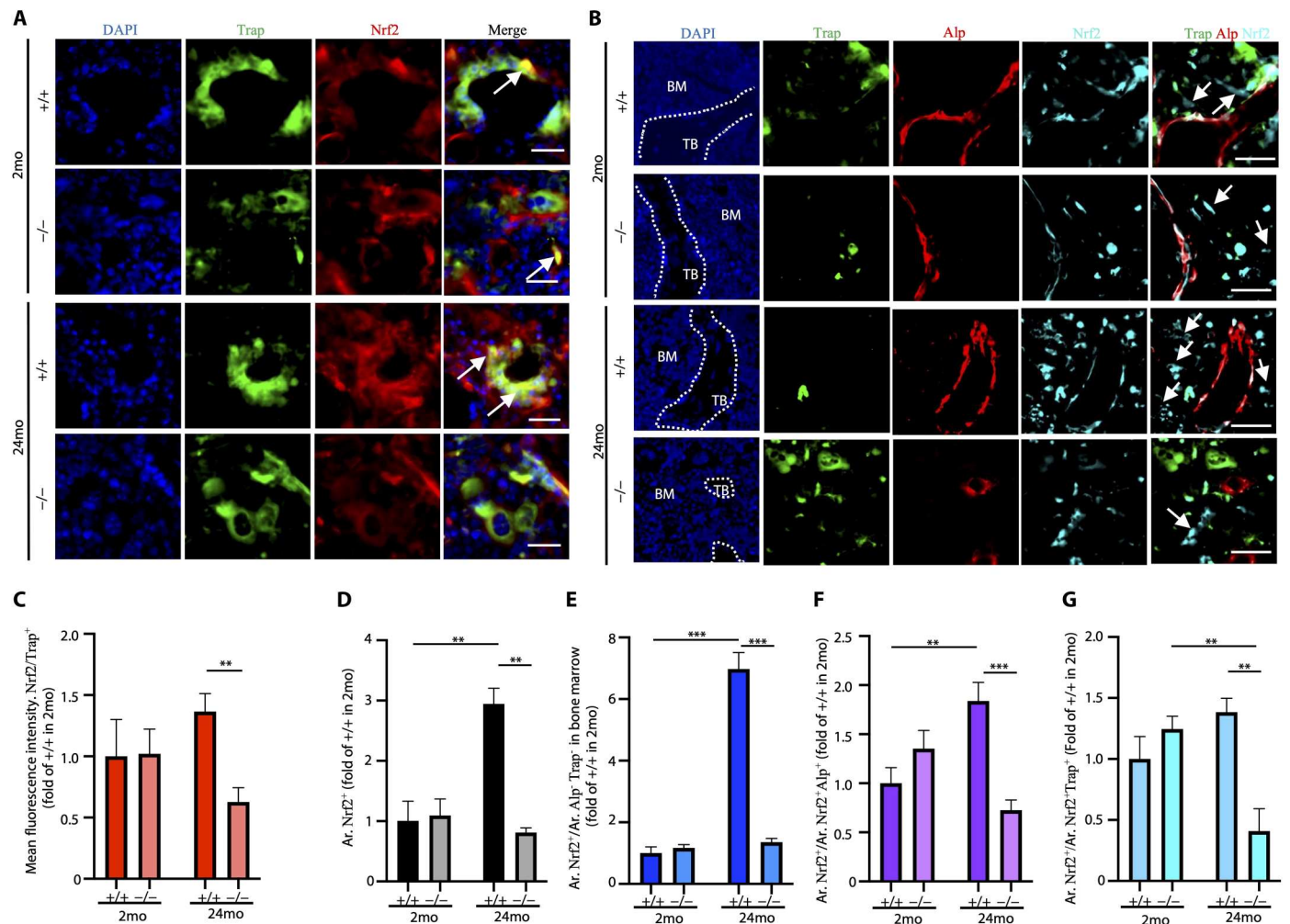
Fig. 2. OPTN modulates NRF2 expression and interacts with the NRF2 regulator KEAP1. (**A**) Immunoblot (IB) analysis of *Optn*⁻/⁻, *Optn*⁺/⁺, and OPTN-overexpressed osteoclasts. β-Actin and histone H3 were used as cytoplasmic and nuclear controls. (**B**) Quantitation of immunoblot in NRF2 and OPTN. (**C**) Representative images of DAPI, OPTN, NRF2, and KEAP1 in primary osteoclasts. Scale bars, 20 μm (low power views) and 5 μm (high power views). (**D**) Coimmunoprecipitation (co-IP) of enhanced green fluorescent protein (eGFP)–OPTN and HA-KEAP1. HA-tag and beads were used as negative and blank controls. (**E**) Representative images showing colocalization of DAPI, OPTN, NRF2, and KEAP1 in the trabeculae and bone marrow from femurs of *Optn*⁺/⁺ animals. High power views of osteoclastic areas (yellow box) and nonosteoclastic areas (blue box) are shown. KEAP1 was further recolored to blue merged with green OPTN and red NRF2 for quantification of OPTN-NRF2 (yellow), OPTN-KEAP1 (cyan), and NRF2-KEAP1 (magenta) colocalization. Scale bars, 50 μm (low power views) and 20 μm (high power views). (**F**) Quantification of the areas of OPTN-NRF2, OPTN-KEAP1, and NRF2-KEAP1 colocalization in osteoclastic and nonosteoclastic areas. Data presented as means ± SD; $n = 3$ experiments; *$P < 0.05$, **$P < 0.01$, and ***$P < 0.001$.

Fig. 3. Deletion of OPTN results in decreased NRF2 in aged osteoclasts and other bone marrow cells. (**A**) Representative images of DAPI, TRAP, and NRF2 colocation show that NRF2 is strongly expressed in TRAP+ osteoclastic areas of femurs, markedly by highly NRF2 expressed areas (Ar. Nrf2high; indicated by arrows) in TRAP+ osteoclastic areas. $n = 3$. Scale bars, 20 μm. (**B**) Representative images showing for localization of DAPI, TRAP, ALP, and NRF2 in femur trabeculae and bone marrow. TRAP was used to show osteoclastic regions, and ALP was used to show osteoblastic regions (contour of trabeculae) in the bone. Scale bars, 50 μm. (**C**) Quantification of average fluorescence intensity of NRF2 in TRAP+ areas. Quantification of fluorescence was performed in different bone marrow regions: (**D**) total NRF2 for all regions, (**E**) NRF2 in nonosteoclastic and nonosteoblastic areas in the bone marrow (Ar. Alp−Trap−; indicated by arrows), (**F**) NRF2 in osteoblastic areas, and (**G**) NRF2 in osteoclastic areas. (C to G) Data presented as means ± SD; $n = 3$ femurs; **$P < 0.01$ and ***$P < 0.001$.

It is unknown how loss of OPTN affects NRF2 in other bone cells. To investigate this, we first analyzed OPTN expression in $Optn^{-/-}$ versus $Optn^{+/+}$ bones using Western blotting with fresh whole bone marrow lysates. We observed approximately 40% decreased NRF2 expression in aged bones following OPTN deletion, although no significant difference was observed between the young samples (fig. S3A). We next investigated NRF2 expression in trabecular bone area covering both trabeculae and bone marrow regions using immunofluorescent staining and confocal microscopy. As previously described, TRAP staining was used to visualize osteoclasts. In contrast, ALP staining was used to visualize osteoblasts that are typically located on the margin of trabecular bone (Fig. 3B), which is differentiated from bone marrow. Results showed that (i) NRF2 signals were more colocalized with TRAP than ALP regardless of genotype or age, suggesting that NRF2 are more expressed in osteoclasts than osteoblasts. (ii) Increased age

significantly increased NRF2 expressions in the bone marrow of normal bones; however, the difference was not significant in the setting of OPTN deletion. (iii) Mature osteocytes that could be found inside trabeculae showed weak NRF2 expression regardless of age or genotype. Further analysis revealed increased general NRF2 expression in normal aged bones (Fig. 3D, threefold increase, $P < 0.01$), particularly in nonosteoclastic, nonosteoblastic cells in the bone marrow (Fig. 3E, sevenfold increase, $P < 0.001$), and in osteoblasts (Fig. 3F, 1.8-fold increase, $P < 0.05$). This increase was not significant in the setting of OPTN deletion. However, NRF2 expression in osteoclastic areas persisted at a high level regardless of age in $Optn^{+/+}$ bones, and deletion of OPTN led to significantly decreased NRF2 expression in aged bones (Fig. 3G). The above findings suggest that NRF2 expression increases with age in multiple bone cells such as nonosteoclastic bone marrow cells and osteoblasts. The increase in NRF2 expression is not observed with deletion of

OPTN. Moreover, it appears that loss of OPTN adversely affects the age-dependent increase in NRF2 expression in all types of bone cells, particularly in the bone marrow.

Deletion of OPTN results in age-dependent increase in intracellular ROS in the bone marrow and osteoclastogenesis in vivo

We next determined whether the difference in NRF2 expression is associated with differences in downstream NRF2-mediated antioxidants and ROS levels. Transcriptional expression of NRF2-mediated antioxidants was assessed through reverse transcription polymerase chain reaction (RT-PCR). Mitochondrial activity contributes to most of the intracellular ROS and can be differentiated from other sources of ROS in a cell's extracellular environment (*14*). Because environmental ROS can easily pass into cells and may affect the accuracy of measuring total intracellular ROS, we used MitoSOX to evaluate mitochondrial ROS in preosteoclasts to distinguish between the two ROS sources.

As expected, lower expression of numerous NRF2-mediated antioxidants, *Gclc*, *Gclm*, *Hmox1*, and *Nqo1* (fig. S3B), was observed in *Optn*$^{-/-}$ osteoclasts by RT–quantitative PCR (qPCR). In addition, higher intracellular mitochondrial ROS (Fig. 4A) and higher intracellular total ROS levels (Fig. 4B) were observed in *Optn*$^{-/-}$ cells compared to *Optn*$^{+/+}$ cells using fluorescence imaging of MitoSOX staining and 2′,7′-dichlorofluorescin diacetate (DCF) assays, respectively. To confirm these findings, we also quantitated intracellular mitochondrial ROS in preosteoclasts from fresh bone marrow using flow cytometry. To identify preosteoclasts, we used known surface markers CD14 and CD265. We initially determined whether there was a difference in the number of baseline preosteoclasts in the bone marrow of *Optn*$^{-/-}$ and *Optn*$^{+/+}$ mice. We did not find any significant differences in the number of CD14$^+$CD265$^+$ preosteoclasts by genotype or age (Fig. 4C). Regarding mitochondrial ROS, significantly increased number of high MitoSOX signal preosteoclasts was observed only in aged *Optn*$^{-/-}$ mice, suggesting a higher intracellular ROS level in these cells (Fig. 4D). These results suggest that a decrease in NRF2 in aged *Optn*$^{-/-}$ mice results in decreased downstream antioxidant expression and an accumulation of intracellular ROS levels produced by the mitochondria during osteoclastogenesis.

In addition to ROS derived from mitochondrial metabolism intracellularly, ROS can also originate from an extracellular source. Bone contains a variety of types of cells with different metabolic activities, for example, erythrocytes and leukocytes in the bone marrow. While mature erythrocytes are mitochondria-free and less metabolically active, leukocytes produce and release ROS as part immune cell physiology. MitoSOX stained with whole bone marrow flushes showed that approximately 20% of bone marrow cells were MitoSOX positive in young mice regardless of genotype. This number stayed the same in normal aged mice but increased to 30% in aged *Optn*$^{-/-}$ mice (Fig. 4E). Because bone marrow cells contain a large number of highly metabolically active leukocytes, we next sought to determine how much leukocytes contribute to ROS accumulation and oxidative stress in bone cells. We performed flow cytometry after MitoSOX staining using leukocytes identified by the CD45 marker from freshly prepared bone marrow samples. Our results confirmed that leukocytes contribute notable ROS in the bone marrow regardless of age or genotype. No significant change was observed between young bones from either *Optn*$^{-/-}$

or *Optn*$^{+/+}$ mice (Fig. 4F). Leukocytes could be further divided into three groups on the basis of their intracellular ROS levels (low, medium, and high). Deletion of OPTN doubled the number of "medium ROS" leukocytes and increased by approximately 20% the number of "high ROS" leukocytes in aged bones (Fig. 4F). Our data from these experiments showed that exogenous ROS from bone marrow leukocytes might also contribute to elevated ROS in *Optn*$^{-/-}$ cells in addition to endogenous mitochondrial sources.

Because ROS has been reported to be an intracellular secondary messenger that mediates the production of osteoclasts, we next determined whether increased ROS in aged *Optn*$^{-/-}$ mice is associated with enhanced osteoclastogenesis. Osteoclasts were differentiated from young and aged mice of both genotypes. We found that *Optn*$^{-/-}$ cells exhibited higher osteoclastogenic activity compared to *Optn*$^{+/+}$ cells, in general, regardless of age (fig. S4A). *Optn*$^{-/-}$ cultures exhibited more mature osteoclasts per area, larger average osteoclast size, and more nuclei per cell (fig. S4B). In addition, gene expression of several key osteoclastogenic markers, including *Nfatc1*, *Mmp9*, and *Tnf*α, was significantly increased in *Optn*$^{-/-}$ versus *Optn*$^{+/+}$ (fig. S4C). These findings were more pronounced in cells obtained from older *Optn*$^{-/-}$ mice (fig. S4). Accordingly, higher osteoclastogenic activity was also observed in aged mice in the setting of OPTN deletion by higher number of osteoclasts in TRAP staining (Fig. 4, G to I) and higher serum C-terminal telopeptide [type I collagen cross-linked C-telopeptide (CTX-1)] levels (Fig. 4J). Young *Optn*$^{-/-}$ bones bore a similarity to aged wild-type bones, as shown by wider distribution of osteoclasts (Fig. 4G) and increased numbers of preosteoclasts (Fig. 4K) in trabecular bones, suggesting that these two conditions may have similar tissue environment for osteoclast development.

Collectively, our data support our working hypothesis that OPTN regulates NRF2 activity in vivo. Loss of OPTN decreases NRF2 expression, which, in turn, decreases the expression of downstream NRF2-mediated antioxidants, increases osteoclastic ROS, and enhances osteoclastogenesis. Our data also suggest that extracellular ROS may be critical for the age-dependent OPTN-associated hyperactivation of osteoclastogenesis in vivo.

Loss of OPTN increases sensitivity to exogenous ROS with increased intracellular ROS production and osteoclastogenesis

We next investigated how extracellular ROS influences oxidative stress and osteoclastogenic activity. After inducing preosteoclasts from aged *Optn*$^{-/-}$ and *Optn*$^{+/+}$ mice, the cells were treated with the incremental amount of hydrogen peroxide ranging from 0 to 200 μM H_2O_2 during osteoclastogenesis induced by RANKL. This system enabled us to manipulate extracellular ROS and determine how this affects osteoclastogenic activity.

TRAP staining (Fig. 5A) showed that incremental extracellular ROS below 100 μM could increase osteoclastogenesis in both *Optn*$^{-/-}$ and *Optn*$^{+/+}$ cells (Fig. 5A). We observed more mature osteoclasts per area, larger average osteoclast size, and more nuclei per cell (Fig. 5B). Notably, *Optn*$^{-/-}$ cells were always of higher osteoclastogenic activity compared to *Optn*$^{+/+}$ cells under the same H_2O_2 treatment below 100 μM. H_2O_2 (200 μM) resulted in even lower osteoclastogenic activity compared to 100 μM treatment, suggesting that there is a certain threshold for extracellular ROS to stimulate osteoclastogenic activity.
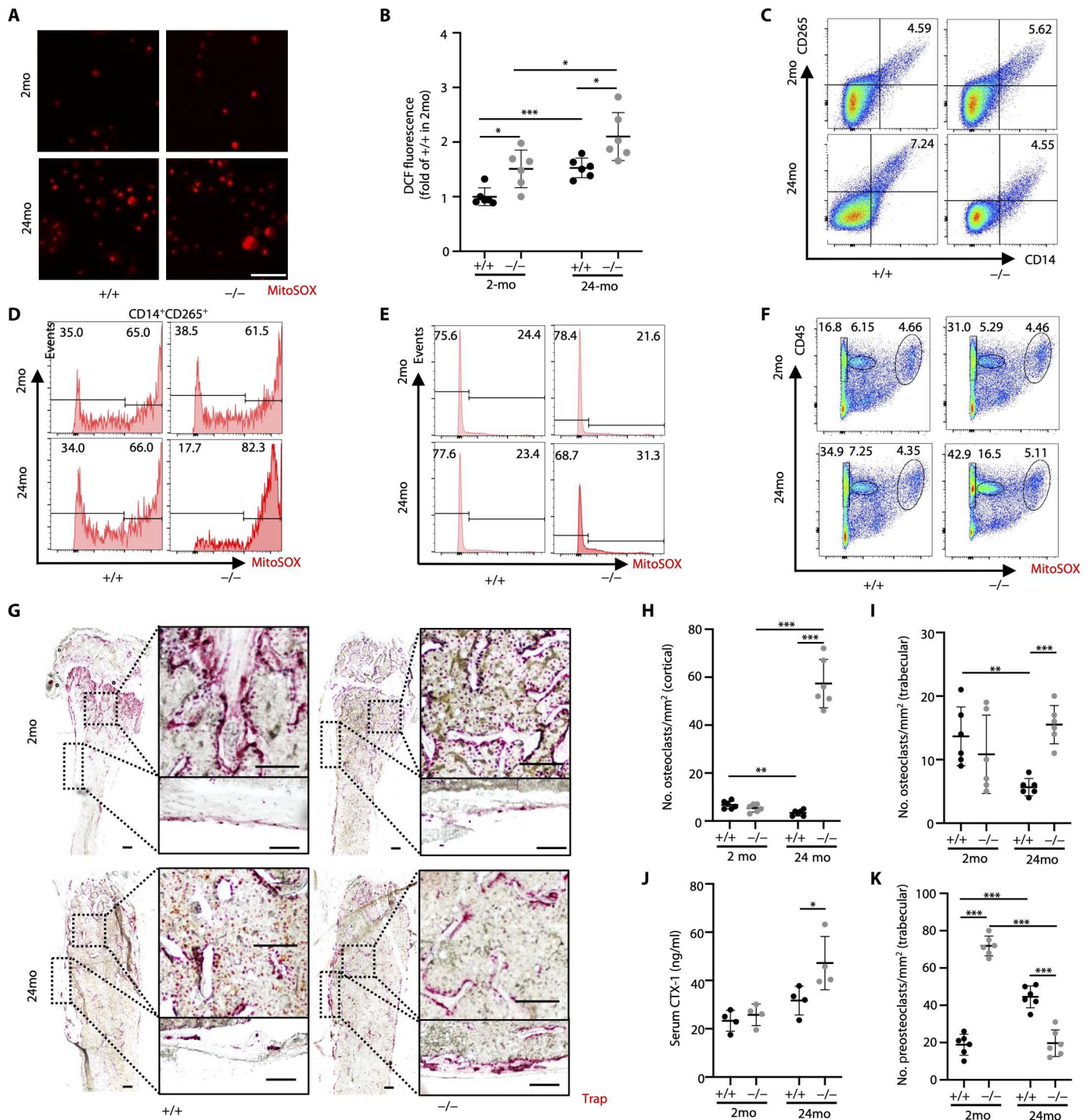
Fig. 4. Deletion of OPTN results in age-dependent increase in intracellular ROS in the bone marrow and osteoclastogenesis in vivo. (**A**) Representative fluorescent images of preosteoclasts stained with MitoSOX. Scale bar, 100 μm. (**B**) Quantification of intracellular ROS of preosteoclasts using DCF ($n = 6$). (**C**) Analysis of the number of preosteoclasts with CD14^{+} and CD265^{+} surface markers ($n = 4$). (**D**) Staining for mitochondrial ROS by MitoSOX in CD14^{+}CD265^{+} preosteoclasts ($n = 4$). (**E**) Staining for mitochondrial ROS by MitoSOX in whole bone marrow cells ($n = 4$). (**F**) Flow cytometry analysis on CD45^{+} leukocytes from fresh bone marrows with MitoSOX staining ($n = 4$). On the basis of mitochondrial ROS level, CD45^{+} leukocytes were further divided into three groups (low, medium, and high). (**G**) Representative images of TRAP staining of femurs (left) and details of trabecular bones (top right) and cortical bones (bottom right). Scale bars, 500 μm. Quantification of osteoclasts numbers in (**H**) cortical bones, (**I**) trabecular bones, and (**K**) preosteoclasts in trabecular bones ($n = 3$ femurs). (**J**) Enzyme-linked immunosorbent assay (ELISA) assay on serum CTX-1 level ($n = 4$). (B and H to K) Data presented as means ± SD; *$P < 0.05$, **$P < 0.01$, and ***$P < 0.001$. (C to F) Data marked by the percentage of cells in %.

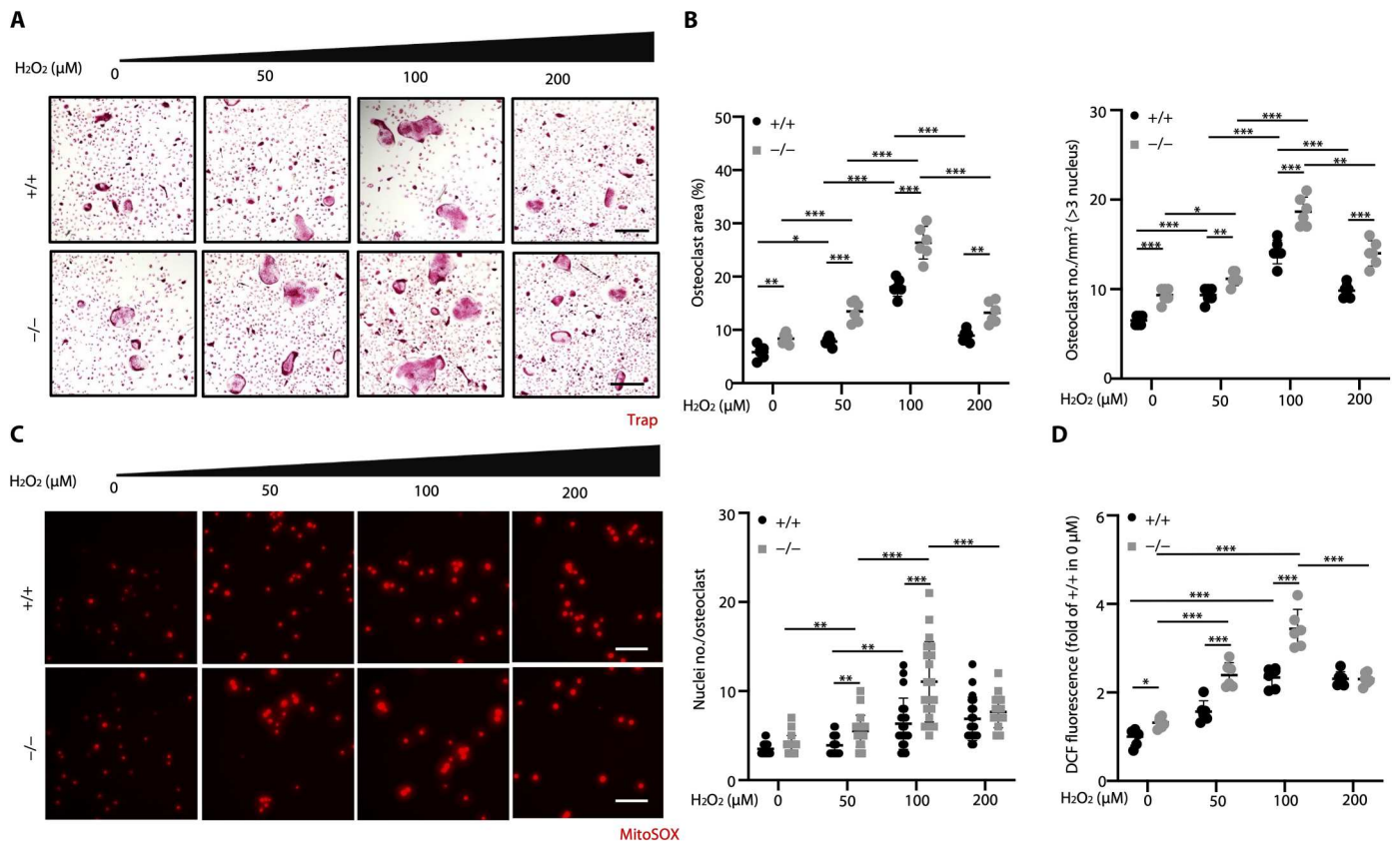**Fig. 5. Loss of OPTN increases sensitivity to exogenous ROS with increased intracellular ROS production and osteoclastogenesis.** (**A**) Representative images of TRAP staining of osteoclasts exposed to H_2O_2 at 0, 50, 100, or 200 μM during osteoclastogenesis (4 days after induction). Scale bars, 200 μm. (**B**) Quantification of osteoclastogenesis based on TRAP staining, by the percentage of osteoclast area per image, osteoclasts number per square millimeter, and nucleus number per osteoclast ($n = 20$ cells per group). (**C**) Representative images for MitoSOX staining of preosteoclasts undergoing osteoclastogenesis (4 days after induction) with H_2O_2 at 0, 50, 100, or 200 μM. Scale bars, 50 μm. (**D**) Quantification of intracellular ROS of preosteoclasts using DCF staining. Data were collected from the cells of 24-month-old $Optn^{+/+}$ or $Optn^{-/-}$ mice. (B and F) Three mice per group; data presented as means ± SD; *$P < 0.05$, **$P < 0.01$, and ***$P < 0.001$.

Using MitoSOX Red staining and fluorescence microscopy, we also observed higher levels of mitochondrial ROS in $Optn^{-/-}$ versus $Optn^{+/+}$ cells, increased with H_2O_2 treatment under 100 μM but decreased at 200 μM H_2O_2 (Fig. 5C). This was confirmed by additional quantitative analysis by assay (Fig. 5D). These findings not only show that aged $Optn^{-/-}$ cells had higher intracellular ROS levels under stress but also suggest that extracellular ROS could further increase intracellular ROS production by mitochondria. This, in turn, increases osteoclastogenesis.

Bone mesenchymal stem cells (BMSCs)/osteoblasts have been reported to regulate osteoclastogenesis through secretory cytokines (26). To rule out the possibility that extracellular ROS is acting on BMSCs/osteoblasts to increase secretion of cytokines, conditional media from cultured BMSCs of either $Optn^{-/-}$ or $Optn^{+/+}$ genotype were collected to treat preosteoclasts of either $Optn^{+/+}$ or $Optn^{-/-}$ genotype during osteoclastogenesis. The results of TRAP staining (fig. S5A) confirmed no change between cells treated with $Optn^{+/+}$ or the $Optn^{-/-}$ conditional media. No differences were observed between mature osteoclasts per area (fig. S5B), average osteoclast size (fig. S5C), and nuclei per cell (fig. S5D).

Collectively, our data suggest that extracellular ROS could markedly increase intracellular ROS, thus up-regulating osteoclastogenic activity. Furthermore, this effect is not due to enhanced cytokine release from BMSCs or osteoblasts.

Deletion of OPTN results in bone tissue oxidative stress with increased age

To further investigate how increased ROS associated with OPTN deletion affects bone tissue, we used fresh bone marrow flushes from aged $Optn^{+/+}$ and $Optn^{-/-}$ mice to assess the extent of oxidative stress induced by ROS. Flow cytometry following CellROX staining and mRNA sequencing (RNA-seq) were performed. CellROX is a fluorescent assay that has been established as an assay for cellular oxidative stress by measuring the extent of ROS binding to DNA (27). Following euthanasia, bone marrow flushes from femurs were dissociated and stained. Fluorescent signals representing relative level of oxidative stress was quantitated using flow cytometry. As expected, the CellROX assay result showed significantly increased level of oxidative stress in aged, $Optn^{-/-}$ bone marrow when compared to $Optn^{+/+}$ ones (Fig. 6A).

Elevated ROS and prolonged exposure can lead to oxidative stress, cellular degeneration, and tissue damage. To determine whether increased ROS resulting from loss of OPTN is causing cellular damage in osteoclasts in the bone, we immunostained bone tissue for TRAP, NRF2, and 8-Hydroxyguanosine (8-OHdG),
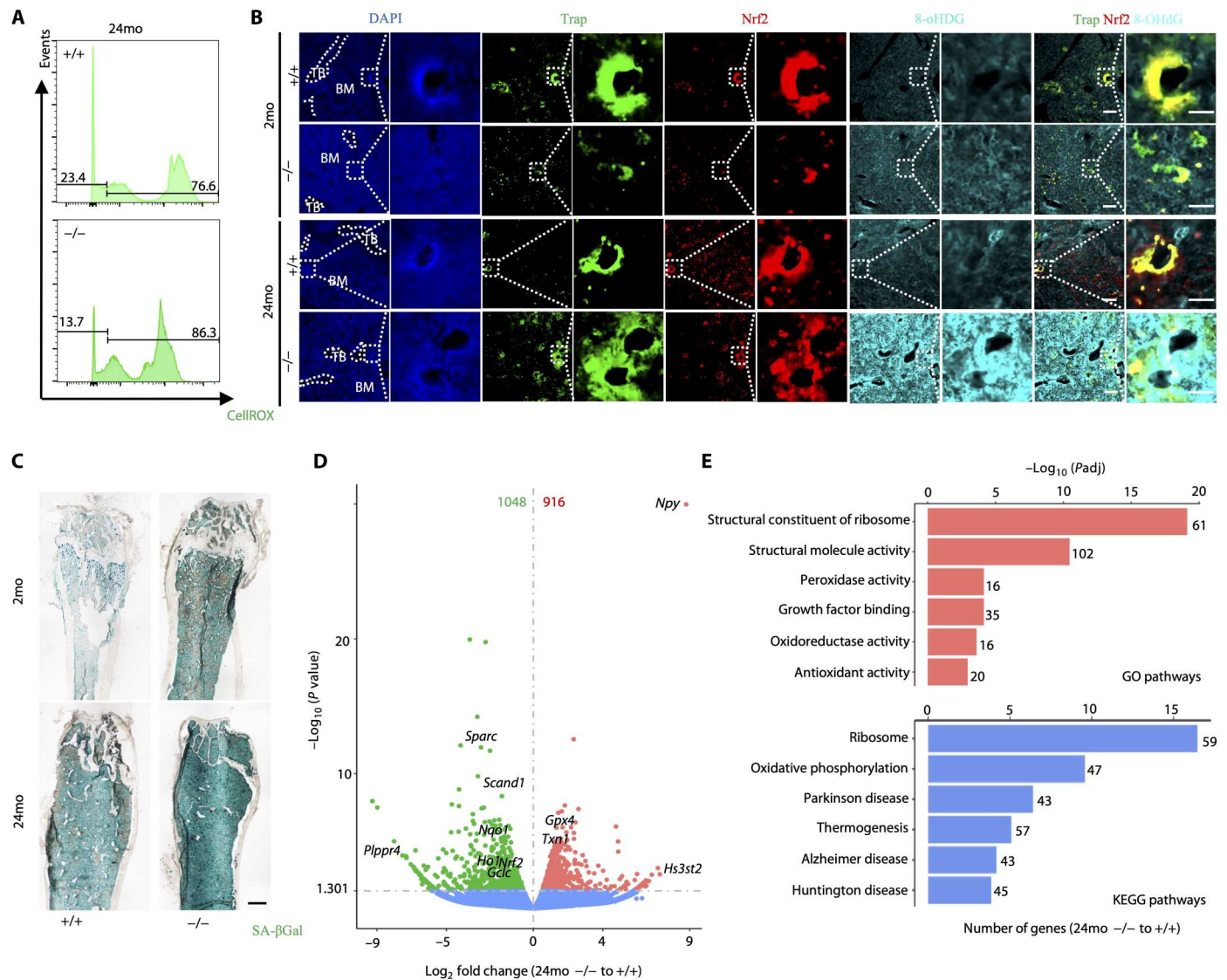
Fig. 6. Deletion of OPTN results in bone tissue oxidative stress with increased age. (**A**) Flow cytometry after staining with CellROX using freshly prepared whole bone marrow from 24-month-old $Optn^{-/-}$ compared to $Optn^{+/+}$ ($n = 4$). (**B**) Representative images of staining for DAPI, TRAP, NRF2, and 8-OHdG in trabecular bones [labeled by trabeculae and bone marrow] in femurs. Detailed views of osteoclastic areas are highlighted and shown to the right for each marker. Scale bars, 50 μm (low power views) and 20 μm (high power views). (**C**) Representative images shown for SA-βGal staining with femurs. Scale bar, 500 μm. (**D**) Volcano plots showed differential expression (DE) of genes in the femur tissues from 24-month-old $Optn^{-/-}$ compared to $Optn^{+/+}$ based on RNA-seq results ($n = 2$ per genotype). Some significantly altered genes are involved in metabolic turnover (Npy, $Hs3st2$, $Sparc$, $Scand1$, and $Plppr4$). NRF2-induced antioxidant genes ($Nrf2$, $Ho1$, $Nqo1$, and $Gclc$) were significantly down-regulated, and alternative antioxidant pathway genes ($Gpx4$ and $Txn1$) were significantly up-regulated. (**E**) Gene Ontology (GO) and Kyoto Encyclopedia of Genes and Genomes (KEGG) analysis for RNA-seq of samples from femur tissue lysates from 24-month-old $Optn^{-/-}$ mice compared to $Optn^{+/+}$ mice; top 6 most changed pathways were plotted.

which is a marker for oxidative damage. Staining was performed in gross bone samples covering both trabeculae and bone marrow (Fig. 6B). Unexpectedly, a high level oxidative damage was observed in young $Optn^{-/-}$ bone. This was as severe as that observed in aged $Optn^{+/+}$ bones. While bones in aged $Optn^{-/-}$ mice also exhibited an extremely high level of oxidative damage, osteoclastic areas showed the least oxidative damage. This suggests that osteoclasts could survive and function in a tissue environment with high oxidative stress.

In addition to oxidative tissue damage, we also tested the level of senescence-associated β-galactosidase (SA-βGal), which has been established as a marker for senescence associated with aging (*28*). As expected, an increase in SA-βGal expression was observed in control $Optn^{+/+}$ mice as a function of age (Fig. 6C). Similarly, in both young and aged $Optn^{-/-}$ bones, strong SA-βGal expression was observed. The staining pattern suggests that young $Optn^{-/-}$ bones were almost as senescent as bones from aged $Optn^{+/+}$ mice.

To determine how increased ROS and oxidative stress in $Optn^{-/-}$ bones alter the expression of various genes, we used mRNA

sequencing to analyze the whole tissue lysis from the bone marrow. We identified 1048 up-regulated genes and 916 down-regulated genes in $Optn^{-/-}$ bones compared to $Optn^{+/+}$ ones (fig. S6A). Various marker genes (*Npy*, *Hs3st2*, *Sparc*, *Scand1*, *Plppr4*, etc.) that have been associated with alteration in oxidative stress were among genes that showed the most change in $Optn^{-/-}$ bones. Consistent with our RT-qPCR results above, we also observed decreased expressions of NRF2-induced antioxidant genes (*Ho1*, *Nqo1*, *Gclc*, etc.). We observed increased expression of genes in alternative antioxidant pathways (*Gpx4*, *Txn1*, etc.) that are not regulated by *Nrf2*, suggesting that a compensatory antioxidant response has been activated (Fig. 6D). Last, both Gene Ontology (GO) and Kyoto Encyclopedia of Genes and Genomes (KEGG) pathway analysis revealed that multiple genes in molecular pathways related to metabolism, mitochondrial function, and numerous degenerative diseases were altered in aged $Optn^{-/-}$ bones (Fig. 6E and fig. S6B).

Together, data from the above experiments showed that elevated ROS induces oxidative stress and cellular damage, resulting in accelerated tissue senescence. Furthermore, high ROS exposure also induced changes at the genetic level, up-regulating and down-regulating genes associated with pathways involves in antioxidant responses, metabolism, and mitochondrial function. Many of these transcriptional changes are consistent with known OPTN functions and associations with neurodegenerative diseases such as amyotrophic lateral sclerosis (ALS) and glaucoma.

Oxidative stress stimulates hyperactive osteoclastogenesis in vivo

Thus far, we have shown that deletion of OPTN decreases NRF2 antioxidant response, which, in turn, increases ROS levels and oxidative stress. However, it is unclear whether oxidative stress can directly lead to increased osteoclastogenesis. To investigate this possible mechanism, we performed an in vivo study in which we induced oxidative stress in young $Optn^{-/-}$ mice.

D-Galactose (D-gal) increases tissue ROS and accelerates the aging process (*29*). We used D-gal to induce oxidative stress in mice through peritoneal injections for 8 weeks in 2-month-old $Optn^{+/+}$ or $Optn^{-/-}$ mice. A control group was injected with saline solution (vehicle). Bones from these mice were stained with TRAP to evaluate osteoclastogenesis. Results were also compared to aged, 24-month-old $Optn^{+/+}$ and $Optn^{-/-}$ mice (Fig. 7A).

While vehicle treatment showed no difference in osteoclasts numbers between $Optn^{+/+}$ and $Optn^{-/-}$ mice (Fig. 7, B, E, and F), D-gal injection in young $Optn^{+/+}$ mice did not enhance osteoclastogenesis. In contrast, D-gal injection resulted in much higher numbers of osteoclasts in young $Optn^{-/-}$ mice compared to $Optn^{+/+}$ controls (Fig. 7, C, E to F). This level was comparable to 24-month-old $Optn^{-/-}$ mice that did not receive any D-gal injection (Fig. 7, D to F). Increased osteoclastic numbers were observed in both cortical and trabecular bones. Enzyme-linked immunosorbent assay (ELISA) on serum bone resorption marker CTX-1 (Fig. 7G) confirmed that D-gal injection resulted in significantly increased bone loss compared to vehicle-treated controls. CTX-1 levels were as high in young D-gal–injected $Optn^{-/-}$ mice as natural aged ones (Fig. 7G). We also analyzed the effects on osteogenesis following D-gal injection. No significant difference in osteoblasts (fig. S7, A and B) and serum bone formation marker procollagen type I N-terminal propeptide (PINP) (Fig. 7H) was found between $Optn^{+/+}$ and

$Optn^{-/-}$ mice, although D-gal and aging led to significantly decreased osteogenesis in both types of mice. Collectively, the data strongly suggest that oxidative stress is critical in OPTN-associated hyperactive osteoclastogenesis.

Antioxidant treatment attenuates bone loss and hyperactive osteoclastogenesis associated with OPTN deletion

Having shown how deficiency of OPTN and compromised Nrf2-antioxidant response might play a role in the development of OPTN-associated bone loss, we next tested whether supplying exogenous antioxidants might help decrease ROS levels and decrease bone loss. Curcumin is a natural antioxidant that has been shown to activate NRF2 and inhibit osteoclastogenesis in vitro (*30*, *31*). Therefore, we hypothesized that treatment with NRF2 activators such as curcumin might alleviate oxidative stress and reduce osteoclastogenesis in the setting of OPTN deficiency (fig. S9A). To test the potential of curcumin for in vivo therapeutic applications, we injected curcumin peritoneally every other day for 6 weeks into 24-month-old $Optn^{-/-}$ mice that exhibit typical PDB-like bone loss. These mice were compared to vehicle [dimethyl sulfoxide (DMSO)]–treated control mice consisting of 24-month-old $Optn^{-/-}$ mice and 24-month-old $Optn^{+/+}$ mice exhibiting regular bone phenotype (Fig. 8A). As expected, the CellROX assay result showed markedly decreased level of intracellular oxidative stress in $Optn^{-/-}$ bone marrow following global delivery of curcumin when compared to vehicle-treated controls, even lower than the 24-month-old $Optn^{+/+}$ mice (fig. S9B).

Our previous study highlighted OPTN-associated bone loss as cortical focal lesion and loss of trabecular pattern, recapitulating PDB histology. X-ray micro–computed tomography (μCT) revealed substantial restorative effects of curcumin on bone quality in treated mice, with decreased cortical resorptive lesions, more condensed cortical bone, and more organized trabecular pattern (Fig. 8B). Hematoxylin and eosin (H&E) staining also revealed active bone remodeling in the trabecular bone following curcumin injection, marked by larger (arrow) and newly formed (triangle) trabeculae (fig. S9C). Furthermore, curcumin treatment significantly improved cortical bone mineral density (Ct. BMD) of the $Optn^{-/-}$ mice to the same level as the $Optn^{+/+}$ controls (Fig. 8C). We observed a decreasing trend in the thickness of cortical bone (Ct. Th) after the treatment, while no difference was observed in cortical area (Ct. A), even between the $Optn^{-/-}$ mice and the $Optn^{+/+}$ controls (Fig. 8C). As expected, we did not observe any change in trabecular bone mineral density (Tb. BMD), trabecular bone volume fraction (Tb. BV/TV), or thickness of trabecular bone (Tb. Th) (Fig. 8C and fig. S9D). However, we did observe decreased trabecular numbers (Tb. Th) and increased trabecular separation (Tb. Sp) (fig. S9D). These changes may be related to the growth of new trabecular bones as shown by the H&E staining (fig. S9C). TRAP staining with the femur slices (Fig. 8D) and quantitative analysis on osteoclasts counting showed that systemic curcumin injection significantly inhibited osteoclastogenesis in $Optn^{-/-}$ mice, especially in Ct. As, marked by approximately 65% decreased osteoclasts numbers in the cortical bone (Fig. 8E) and 40% lower osteoclasts numbers in the trabecular bone (Fig. 8F) compared to the vehicle-treated ones. This pattern was confirmed by ELISA assay on serum CTX-1, which showed a significant decrease in osteoclasts
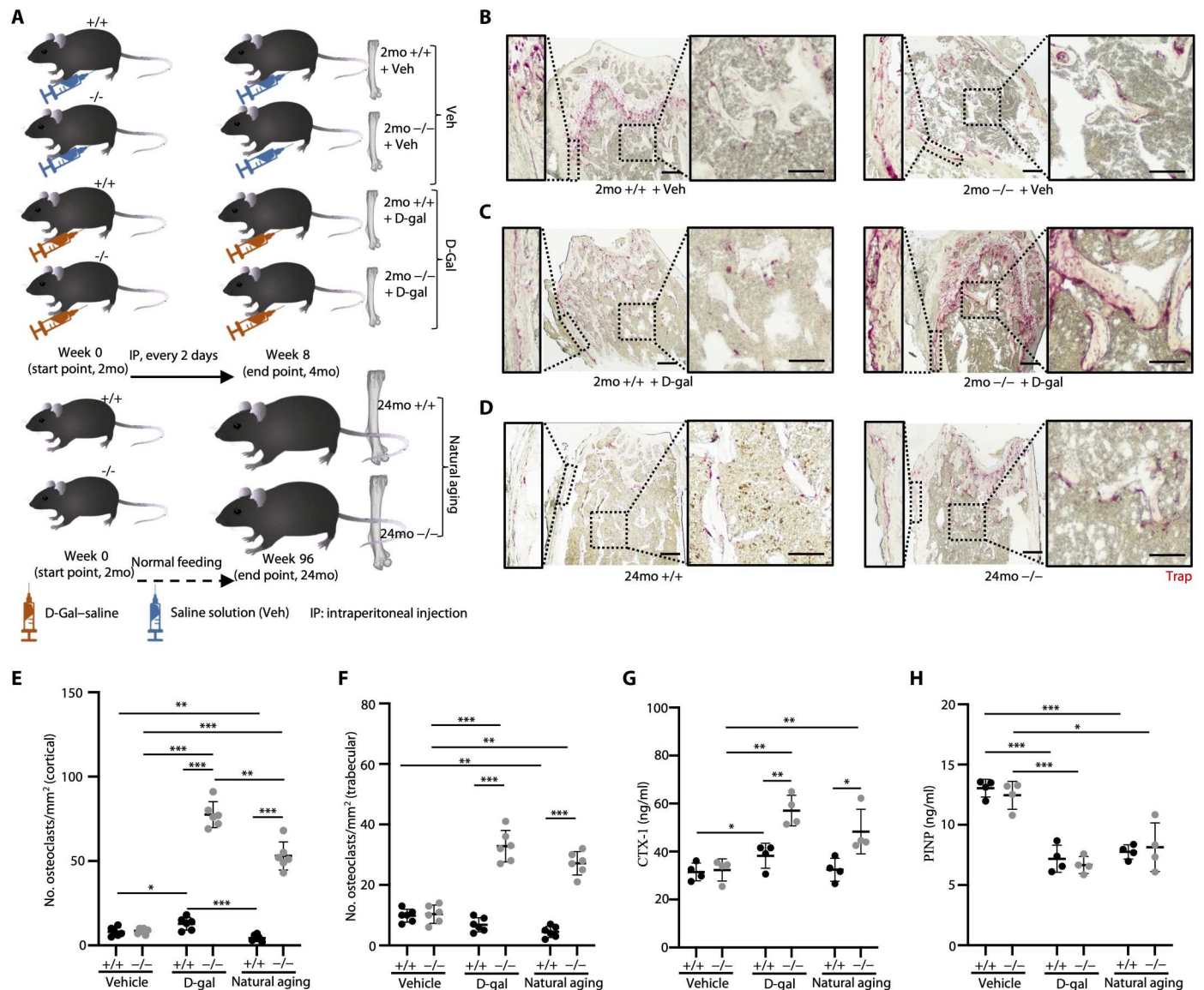
Fig. 7. Oxidative stress stimulates hyperactive osteoclastogenesis in vivo. (**A**) Schematics for in vivo experiments to induce osteoclastogenesis in 2-month-old *Optn*^{+/+} and *Optn*^{−/−} mice; negative control groups received an injection of saline (Veh); natural aging group for positive control (*n* = 4 mice per group). Bones were then stained for TRAP to identify osteoclasts in femurs in (**B**) Veh groups, (**C**) D-gal groups, and (**D**) natural aging groups. Scale bars, 200 μm (low power views) and 100 μm (high power views). Quantification of osteoclasts numbers in (**E**) cortical bones or (**F**) trabecular bones (*n* = 4). (**G**) ELISA assay on serum CTX-1 level (*n* = 4). (**H**) ELISA assay on serum PINP level (*n* = 4). (E to H) Data presented as means ± SD; *P < 0.05, **P < 0.01, and ***P < 0.001

in curcumin-treated *Optn*^{−/−} mice to the level of *Optn*^{+/+} normal mice (Fig. 8H).

We further characterized curcumin-treated *Optn*^{−/−} mice by staining femurs for TRAP, ALP, and NRF2. We observe significantly increased NRF2 expressions in curcumin-treated groups (Fig. 8G, Nrf2 column). The curcumin-treated bones showed significantly increased activity of ALP for osteogenesis (Fig. 8G, Alp column), compared to their vehicle-treated controls, as well as *Optn*^{+/+} normal bones, although no significant difference in osteoblasts (fig. S8A) and serum bone formation marker PINP (fig. S8B) was found between *Optn*^{+/+} and *Optn*^{−/−} mice. This suggests that curcumin treatment did not only inhibit osteoclastogenesis but also promoted active remodeling of bone. Serum ELISA assay

confirmed significantly increased PINP in *Optn*^{−/−} mice following curcumin treatment compared to vehicle-treated *Optn*^{−/−} and *Optn*^{+/+} mice (Fig. 8I). However, curcumin did not prevent oxidative damage in aged *Optn*^{−/−} mice, as shown by 8-OHdG expression that remained unchanged following curcumin treatment (fig. S9E). Together, these results suggest that treatment with an antioxidant such as curcumin ameliorated OPTN-associated bone loss.

DISCUSSION

Degenerative diseases affect millions of elderly people around the world resulting in substantial pain, suffering, and health care costs (*1*). Central nervous system and skeletal systems are most
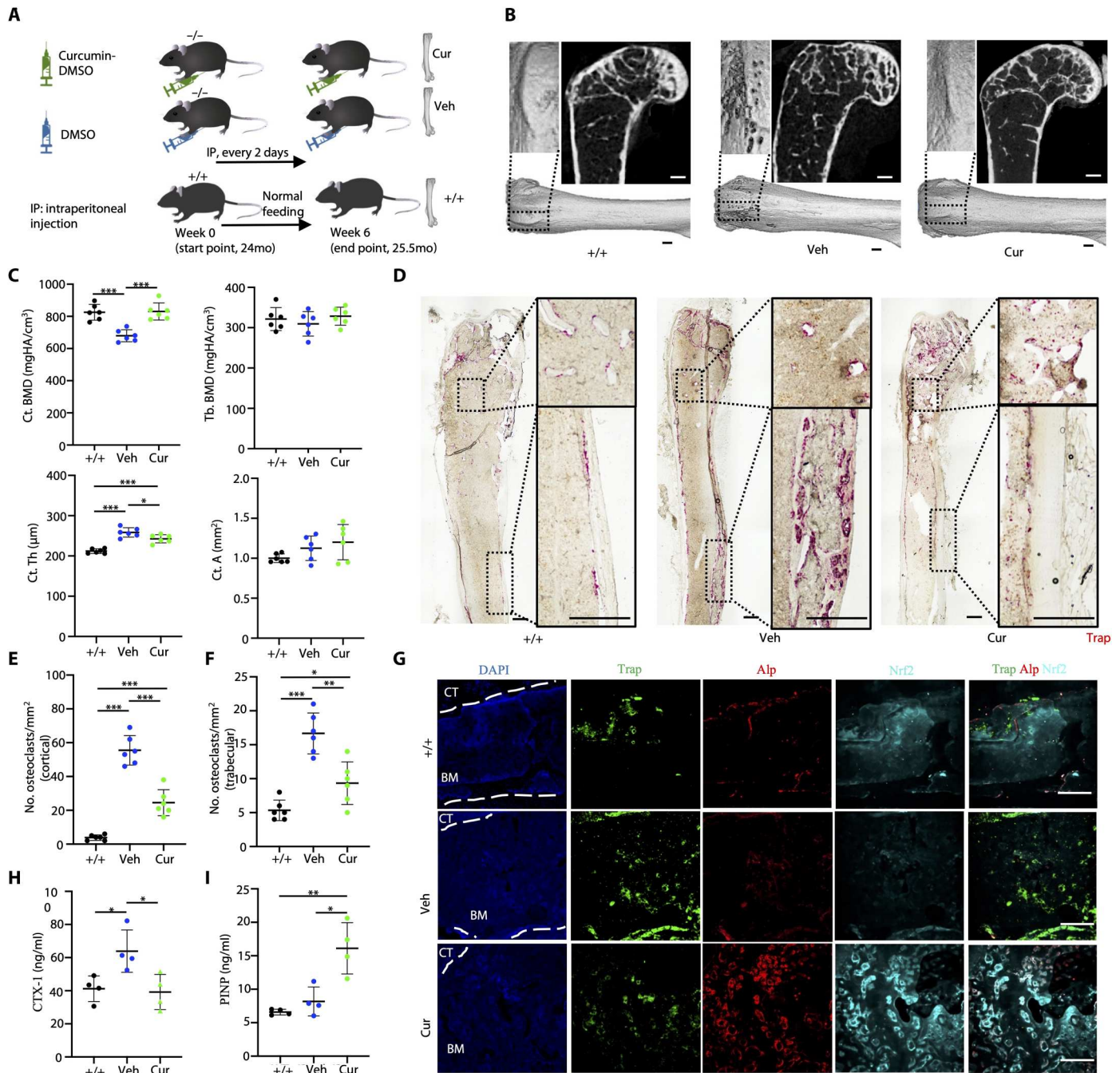
Fig. 8. Antioxidant treatment attenuates bone loss and hyperactive osteoclastogenesis associated with OPTN deletion. (**A**) Schematics for in vivo experiments to restore PDB-like phenotypes in 24-month-old *Optn*−/− mice. Twenty-four–month-old *Optn*−/− mice were peritoneally injected with curcumin. Twenty-four–month-old *Optn*−/− mice injected with DMSO (Veh) served as negative controls. Twenty-four–month-old *Optn*+/+ mice were included as normal control animals for comparison [*n* = 6 mice per group (one in Veh group and one in Cur group died at week 5)]. (**B**) Representative μCT scanning and three-dimensional reconstruction images of cortical bone for focal resorptive lesions. Scale bars, 500 μm. (**C**) Quantification of cortical bone mineral density (Ct. BMD), trabecular bone mineral density (Tb. BMD), thickness of cortical bone (Ct. Th), and (**G**) area of cortical bone was performed. (**D**) Representative imaging of TRAP staining of femurs (left) with high magnification views for trabecular bones (top right) and cortical bones (bottom right). Scale bars, 500 μm. Quantification of TRAP+ osteoclasts numbers in (**E**) cortical bones or (**F**) trabecular bones is shown. (**G**) Representative images of DAPI, TRAP, ALP, and NRF2 in femurs, with cortical (CT) and bone marrow. Scale bars, 200 μm. (**H**) ELISA assay on serum CTX-1 level. (**I**) ELISA assay on serum PINP level (*n* = 4). (C and E to H) Data presented as means ± SD; *$P < 0.05$, **$P < 0.01$, and ***$P < 0.001$.

susceptible to age-dependent degeneration (2–4). OPTN has been implicated in numerous neurodegenerative diseases and was recently identified to be genetically associated with PDB, the second most prevalent degenerative bone disease (5–8). Efforts to uncover the mechanism(s) underlying OPTN-associated degeneration have been limited to nuclear factor κB and interferon signaling pathways in osteoclasts (11, 32). Our previous in vitro work showed that OPTN modulates ROS in osteoclasts by direct interaction with NRF2 (12). In this study, we further extended this study through in vivo work showing that (i) OPTN and NRF2 expression increases with age; (ii) OPTN and NRF2 strongly colocalize in bones; (iii) OPTN modulates Nrf2-induced antioxidant through binding to KEAP1 in various bone tissues; (iv) deficiency of OPTN results in compromised Nrf2-induced antioxidant response; (v) deficiency of OPTN results in higher osteoclastic intracellular ROS in aged bones; (vi) deficiency of OPTN leads to increased tissue oxidative stress, which triggers hyperactive osteoclastogenesis by further increasing osteoclastic intracellular ROS; and (vii) we showed that antioxidant treatment could attenuate in vivo hyperactive osteoclastogenesis and bone loss resulting from deletion of OPTN. Our data describe an OPTN pathway for regulating oxidative stress that we call the "OPTN-NRF2 axis" and demonstrate how dysregulated OPTN-NRF2 axis results in hyperactive osteoclastogenesis and OPTN-associated bone loss (Fig. 9).

Generated as the byproduct of energy metabolism, ROS diffuse and pass through cell membranes as a secondary messenger for various cellular processes, such as osteoclastogenesis (14, 16, 33). However, if not properly neutralized by antioxidants, then excessive ROS leads to oxidative stress, cell and tissue damage, or even cell death (19, 34). We found deletion of OPTN leads to notably increased intracellular oxidative stress in osteoclasts. This oxidative stress is exacerbated by extracellular sources of ROS. These phenomena were observed regardless of age in vitro but only in aged situation in vivo. These findings underscore the importance of tissue environment, particularly the extracellular ROS, in the regulation of osteoclasts and pathogenesis of the OPTN-associated pagetic lesions. For example, we found that leukocytes in the bone marrow are a major resource of ROS in aged mice. Dysfunction of OPTN leads to markedly increased ROS level in these cells and leads to tissue oxidative stress in aged bones.

Tissue oxidative stress, rather than osteoclastic intrinsic pathways, appears to be the primary driver for an age-dependent bone lesion in our OPTN mouse model. Our findings show that young $Optn^{-/-}$ bones are similar to aged $Optn^{+/+}$ bones in many aspects, including distribution of osteoclasts, level of oxidative damage, and expression of SA-βGal as an indication of senescence. These findings imply the important role of oxidative stress in the age-dependent pathogenesis of pagetic lesions. Other groups also have found that unbalanced ROS is a critical mediator in numerous metabolic/degenerative bone diseases, including bone aging, postmenopausal osteoporosis, osteoarthritis, and diabetic bone fragility (20, 35–39). However, to our knowledge, no other study has associated ROS/
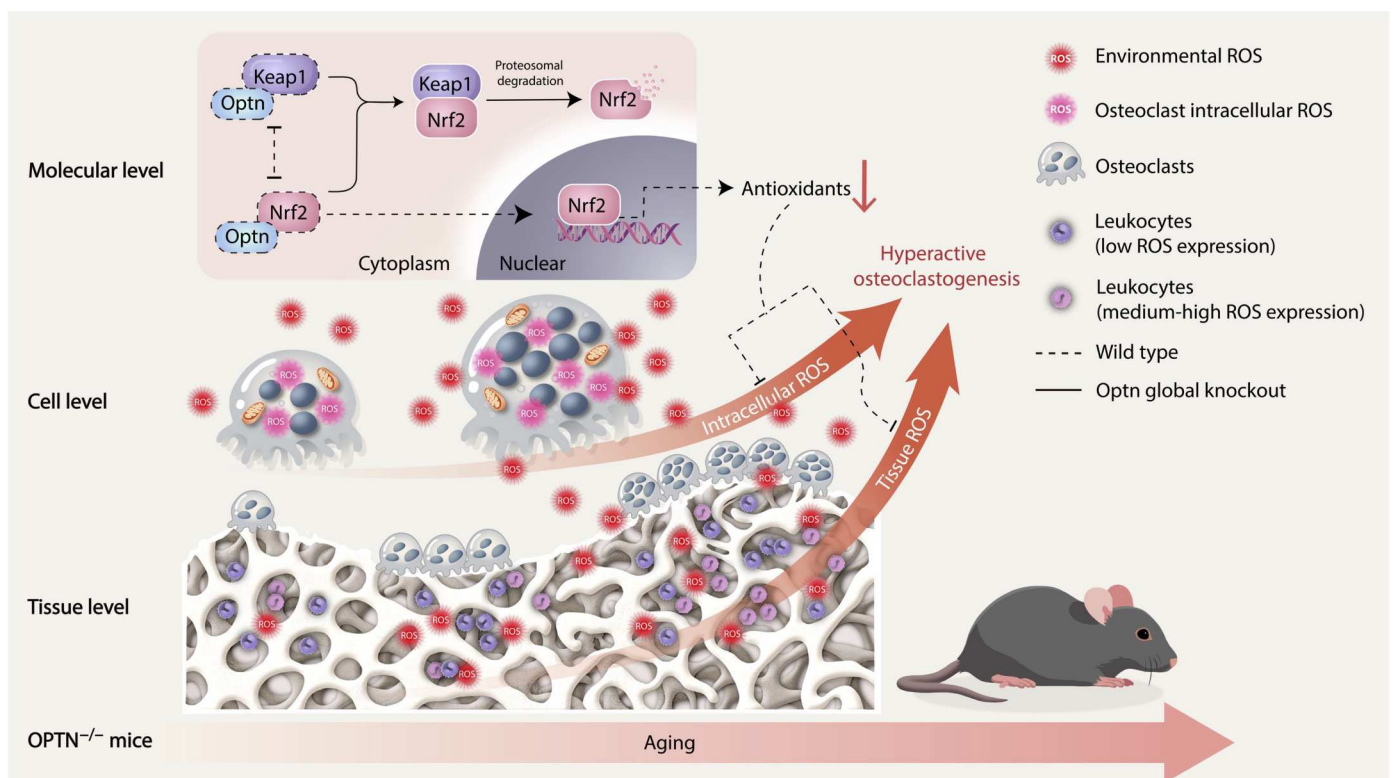

Fig. 9. OPTN-NRF2 axis in the pathogenesis of hyperactive osteoclastogenesis in aged $Optn^{-/-}$ mice. Deletion of OPTN results in increased NRF2-KEAP1 binding, leading to more NRF2 degradation and less NRF2 nuclear translocation, thus compromising NRF2-induced antioxidant response. In aged $Optn^{-/-}$ bones, compromised NRF2 results not only in higher intracellular ROS in preosteoclasts but also in other bone marrow cells such as leukocytes. Increased ROS results in oxidative stress and ultimately enhances osteoclastogenesis in aged $Optn^{-/-}$ mice.

oxidative stress with hyperactivation of osteoclasts in other PDB animal models. An implication of this finding is that OPTN may play an important role in reducing oxidative stress. This is not unexpected since OPTN has been implicated to protect against oxidative stress in neurons (40, 41).

ROS homeostasis is maintained by cellular antioxidant responses. The Nrf2-induced antioxidant response is the primary system to neutralize intracellular ROS and maintain homeostasis (23). NRF2 is constitutively expressed and suppressed in cells. At basal levels, NRF2 is inhibited by binding to its negative regulator, KEAP1, which results in NRF2's degradation. With increased ROS levels, KEAP1 dissociates from NRF2, which is then able to enter the nucleus and induce the expression of downstream antioxidants (23–25). Thus, a decrease in NRF2-KEAP1 binding and an increase in NRF2 expression suggest higher activity of NRF2-induced antioxidant response. Previous reports only suggested that OPTN regulates NRF2 in vitro and potentially through OPTN-NRF2 binding. Consistent with that hypothesis, this study reveals that OPTN is highly colocalized with NRF2 in various types of bone cells in vivo. This study also advances our knowledge by showing that OPTN binds to KEAP1 and that NRF2 is not required for the OPTN-KEAP1 binding. In particular, we find that these bindings increase, synchronous with reduced NRF2 degradation, increased the availability of NRF2 in the cytoplasm, and markedly increased NRF2 into nuclei when OPTN is overexpressed. Together, OPTN-NRF2 and OPTN-KEAP1 binding could be a mechanism for how OPTN regulates NRF2-induced antioxidant response. Future work will be required to elucidate the binding sites and uncover the molecular mechanism of how these bindings regulate NRF2 and downstream antioxidant response.

Although further trials are needed, our study demonstrated the therapeutic potential of antioxidant treatment for OPTN-associated bone degeneration. Except for the pain relief effect of ascorbic acid, no study has discussed the therapeutic potential of antioxidant treatment for PDB (42, 43). We found that antioxidant treatment activates osteogenesis in addition to inhibiting osteoclastogenesis, although osteogenesis was not substantially regulated by deletion of OPTN in $Optn^{-/-}$ mice. Our fluorescent staining data suggest that OPTN and NRF2 likely play greater roles in osteoclasts than other bone cell types. However, the current study could not answer whether the therapeutic effects on osteoclasts could be secondary to effects on osteoblast or other tissues. Osteoblasts have been reported to be susceptible to oxidative stress, and increasing age is associated with a decrease in osteogenesis due to oxidative stress (44, 45). On one hand, curcumin has been reported to induce osteogenesis (46, 47), which leads to rebuilding of bone mass in aged $Optn^{-/-}$ mice. On the other hand, increased osteoblasts could also induce osteoclastogenesis and rapid bone turnover due to osteoblast-osteoclast (OB-OC) coupling (48). Our study suggests that osteoclastogenic activity is inhibited, and osteoblasts have markedly increased NRF2 level in aged $Optn^{-/-}$ mice following curcumin treatment. Thus, it is possible that osteoblast activity is inhibited in aged $Optn^{-/-}$ bones and antioxidant treatment unleashes osteoblast-mediated remodeling. Future studies are needed to elucidate the role of osteoblasts in the pathogenesis of OPTN-associated bone degeneration.

ROS has been implicated in numerous neurodegenerative diseases beyond skeletal tissue. OPTN has also been genetically associated with neurodegeneration in glaucoma and ALS (5, 6). OPTN protein has also been implicated in other neurodegenerative diseases such as Alzheimer's and Parkinson's diseases (44, 45, 49). In these neurodegenerative diseases, oxidative stress has been suggested to trigger neuronal death (44, 50–52). Therefore, our findings on OPTN and NRF2's role in regulating ROS homeostasis and oxidative stress may also contribute to advancing the understanding of pathogenesis of glaucoma, ALS, and other neurodegenerative diseases.

MATERIALS AND METHODS
Study design
The objective of this study was to elucidate the mechanisms and roles of NRF2 antioxidant pathway in the pathogenesis of OPTN-associated bone degeneration. The activity of the NRF2 pathway was first assessed in vivo in both young and aged $Optn^{+/+}$ mice using tissue staining and Western blotting. Further molecular biological studies by plasmid transfection, co-IP, and staining revealed the strong association between OPTN and NRF2 pathway both in vitro and in vivo. Furthermore, young (2-month-old) and old (24-month-old) global OPTN knockout ($Optn^{-/-}$) mice were compared to wild-type ($Optn^{+/+}$) mice for elucidating the pathogenic mechanisms. In these studies, NRF2 pathway, ROS level, oxidative stress, and osteoclastogenic activity were evaluated by various tissue staining, plate reader and flow cytometry–based assays, RNA-seq, etc. Last, D-gal was used to induce tissue ROS, and curcumin was used to induce NRF2 antioxidant response. The treatments were applied through intraperitoneal injection either to induce hyperactive osteoclastogenesis in young $Optn^{-/-}$ mice or to ameliorate bone loss in old $Optn^{-/-}$ mice. μCT, various tissue staining, and ELISA assays were used to evaluate the therapeutic potential of antioxidant treatment for OPTN-associated bone loss. Most data were acquired from at least three independent samples (3 mice or ≥4 for animal experiments). The RNA-seq data were from two biological replicates. All experiments were performed with appropriate controls, and animals were assigned randomly to various experimental/control groups.

Animals
Global Optn knockout ($Optn^{-/-}$) mice on a C57BL/6 background were generated by crossing $Optn^{flox/flox}$ mice with CMV-Cre mice (Jackson Laboratories, Bar Harbor, ME) as described in our previous study. For D-gal–induced aging treatment, 2-month-old male mice of either $Optn^{+/+}$ or $Optn^{-/-}$ genotype were intraperitoneally injected with D-gal (G0750, MilliporeSigma) at the concentration of 200 mg/kg in 200 μl of saline solution every 2 days for 6 weeks (D-gal) compared to 200 μl of saline solution–treated male mice of same genotype (Veh). For antioxidant treatment, 24-month-old $Optn^{-/-}$ male mice were intraperitoneally injected with curcumin (C1386, MilliporeSigma) at a concentration of 25 mg/kg in 200 μl of DMSO every 2 days for 6 weeks (Cur) compared to 200 μl of DMSO-treated $Optn^{-/-}$ male mice of same age (Veh). All animal procedures were approved by the Institutional Animal Care and Use Committees at the Ohio State University, the University of North Carolina at Chapel Hill, and Duke University.

Primary cell culture
Eight-week-old or 24-month-old $Optn^{-/-}$ and $Optn^{+/+}$ mice were euthanized by CO_2, and tibias and femurs were collected. For

osteoclast differentiation, bone marrow cells were flushed out into α–minimum essential medium (α-MEM; #41061029, Gibco) containing 10% fetal bovine serum (FBS; 26140079, Gibco) and penicillin/streptomycin (#15140122, Gibco) and cultured at 37°C in a humidified 5% CO_2 atmosphere. After 1 day, nonadherent cells were collected and reseeded at the concentration of 2×10^5 cells/ml with macrophage colony-stimulating factor (M-CSF; 60 ng/ml; #416ML050, R&D Systems) for 3 days to grow osteoclast precursor cells. For primary culture of BMSCs, bone marrow cells were flushed out into α-MEM (#12571063, Gibco) containing 10% FBS (26140079, Gibco) and penicillin/streptomycin (#15140122, Gibco) and cultured at 37°C in a humidified 5% CO_2 atmosphere. After 3 days, nonadherent cells were discarded, and adherent cells were cultured by changing the same culture medium every 2 days until passaging at 80% confluency. Passage 2 cells were identified by confirming stem cell surface markers through flow cytometry and used for further osteogenic differentiation.

Osteogenic/osteoclastogenic differentiation

To promote osteoclastogenic differentiation, osteoclast precursors were treated with osteoclast α-MEM culture medium containing RANKL (#462TR010, R&D Systems) at 20 ng/ml and M-CSF (#416ML050, R&D Systems) at 60 ng/ml for 6 days until fully differentiated. To promote osteogenic differentiation, BMSCs were cultured with osteogenic media [BMSC culture media containing ascorbic acid (50 μg/ml; PHR1008-2G, MilliporeSigma), 10 mM β-glycerophosphate (G9422, MilliporeSigma), and 10 nM dexamethasone (D4902, MilliporeSigma)]. Osteogenic media from different BMSCs were collected as OB conditional media for analyzing OB-OC cross-talk.

Cell transfections and treatments

mOPTN (MG53387-UT, SinoBiological) overexpression plasmids were transfected to preosteoclasts cells from $Optn^{+/+}$ mice using Lipofectamine LTX Reagent with PLUS Reagent (A12621, Invitrogen) following the manufacturer's instructions. The transfected cells were compared to nontreated $Optn^{+/+}$ preosteoclast cells and preosteoclast cells from $Optn^{-/-}$ mice for further analysis. si$Nrf2$ (s70521, Thermo Fisher Scientific) were transfected to preosteoclasts from $Optn^{+/+}$ mice using Lipofectamine RNAiMAX Reagent (13778030, Invitrogen) following the manufacturer's instructions. The transfected cells were compared to nontreated $Optn^{+/+}$ preosteoclasts.

Reverse transcription quantitative polymerase chain reaction

Total mRNA of osteoclast precursor cells was extracted using RNAzol and reverse-transcribed using the iScript Kit. Subsequently, PCR reactions were prepared using the iTaq Universal SYBR Green Supermix and performed on the StepOnePlus Real-Time PCR System (Applied Biosystems). Primers for target genes are listed in table S1. Threshold cycles of primers were normalized to a housekeeping gene β-actin, and the relative values were calculated on the basis of comparative C_t method ($2 - \Delta\Delta C_t$ method) (12).

Western blot

Protein samples were prepared either by radioimmunoprecipitation assay buffer (R0278, Sigma-Aldrich) to yield total protein or by the Nuclear Extraction Kit (catalog no. 2900, MilliporeSigma) to yield cytoplasmic and nuclear protein. The total protein concentration of each sample was tested and normalized using Pierce BCA Protein Assay Kit (#23225, Thermo Fisher Scientific). The Criterion Vertical Electrophoresis Cell and Trans-Blot Turbo Transfer System (Bio-Rad) were used for immunoblot analysis as described in our previous study. Protein expression levels were detected by ECL Prime Western Blotting Detection Reagent (GE Healthcare Amersham). Antibodies and their working concentrations are listed in table S2.

Co-IP assays

pOPTN-eGFP (#27052), pcDNA3-HA2-Keap1 (#21556), and pHA-tag (#55182) were purchased from addgene.org. For expressed co-IP assay, HEK293T cells were seeded in six-well plates until 80% confluency and transfected with indicated plasmids at a concentration of 2000 ng per plasmid per well by Lipofectamine 2000 according to the manufacturer's protocol. Transfected cells were lysed by NP-40 buffer and split into two parts—200μl fractions for input assay and an 800 μl of fractions for co-IP. The input lysates were resolved on SDS–polyacrylamide gel electrophoresis (PAGE) gels and analyzed by immunoblot. The co-IP lysates were incubated with 20 μl of EZview Red Anti-HA Affinity Gel (E6779-1ML, MilliporeSigma) for 24 hours. For endogenous co-IP assay, osteoclasts from 2-month-old $Optn^{+/+}$ mice were used. The co-IP lysates were precipitated with anti-KEAP1 antibody (sc-514914, Santa Cruz Biotechnology) or normal mouse immunoglobulin G control (#02-6502, Invitrogen) bound to protein G and protein A agarose beads (IP05, MilliporeSigma), respectively, for 24 hours. After the incubation, samples were centrifuged at 5000g for 1 min, and pellets were washed five times with NP-40 buffer. The proteins were lastly resolved on SDS-PAGE gels and analyzed by immunoblot.

Measurement of ROS

Qualitative and quantitative analyses of intracellular/mitochondrial ROS in cells were performed by fluorescence microscopy using MitoSOX Red Mitochondrial Superoxide Indicator (#M36008, Invitrogen) following the user's manual. The stained cells were imaged using an Eclipse Ti microscope (Nikon, Shinagawa, Japan). Cell ROS levels were also assessed by plate reader using DCF (#4091-99-0, MilliporeSigma).

Flow cytometry

Bone marrow cells were measured by flow cytometry to analyze cell types and measure ROS level. Bone marrow flushes were diluted in 1 ml of phosphate-buffered saline (PBS) and stained with different Fc-applicable primary antibodies for 10 min, followed by and 1 μM CellROX Green Reagent (#C10444, Invitrogen) to test generic ROS level or 1 μM MitoSOX Red Mitochondrial Superoxide Indicator (#M36008, Invitrogen) to test intracellular/mitochondrial ROS level for another 20 min. Antibodies and their working concentrations are listed in table S2. The cells were washed three times with PBS before running by flow cytometry and analyzed by FlowJo.

mRNA sequencing and bioinformatic analysis

Total RNA was extracted using an RNeasy mini kit (#74104, QIAGEN). A cDNA library was prepared using NEBNext Ultra DNA library prep kit (E7370L, New England Biolabs), and mRNA sequencing was performed on the NovaSeq 6000 System

(Illumina). RNA-seq data from eight samples were collected: Two replicates in four sample groups (total RNA from fresh bone marrow flushes of 24-month-old $Optn^{-/-}$ and $Optn^{+/+}$ mice were extracted and grouped as aged $Optn^{+/+}$ and aged $Optn^{-/-}$. Reads were mapped to *Mus musculus* mm10 genome by STAR software. Fragments per kilobase of transcript per million mapped reads were calculated to estimate gene expression levels. Differential expression (DE) analysis was performed using the DESeq2 package in R software (version 2_1.6.3) to identify the significant DE genes in the comparisons. *P* values were adjusted using the Benjamini and Hochberg's approach for controlling the false discovery rate. Gene set enrichment tests were performed using the clusterProfiler package and the "camera" function in limma package in R software to test gene sets in MsigDB collection including GO and KEGG (*53*).

Micro–computed tomography
Femurs were dissected from mice free of soft tissue, fixed overnight in 4% paraformaldehyde, and analyzed by high-resolution μCT (Skyscan 1172-D, Kontich, Belgium) with 10-μm^3 voxel size (50 kVp, 200 μA, 0.4° rotation per projection, eight frames averaged per projection, and 260-ms exposure time) and NRecon reconstruction software. Trabecular bone region of interest (ROI) was drawn starting from 5% of femoral length proximal to distal epiphyseal growth plate and extended proximally for a total of 5% of femoral length. The trabecular bone was segmented from the bone marrow and analyzed to determine the Tb. BV/TV, Tb. BMD, Tb. Th, Tb. N, and Tb. Sp. Diaphyseal cortical bone ROI was drawn starting from 20% of femoral length proximal to distal epiphyseal growth plate and extended proximally for a total of 10% of femoral length. We analyzed the cortical bone to determine the Ct. Th, Ct. A, and Ct. BMD.

ELISA assays
Serum-based ELISA assays were performed to test serum levels of PINP and CTX-1. Whole blood from various mice models were collected through cardiac puncture. Blood samples were then kept still at 4°C overnight, followed by centrifuging at 3000 rpm for 15 min. Blood was stratified, and serum from top layer was carefully collected for ELISA assays. The Mouse PINP ELISA Kit (MBS2500076, MyBioSource) and the Mouse CTX-I ELISA Kit (MBS2700259, MyBioSource) were used following the manufacturer's protocol.

Cell and tissue staining
For TRAP staining, the staining solutions were prepared following previously published standard protocol. Cells were fixed with 10% paraformaldehyde for 10 min before incubating in TRAP staining solution for 10 min at 37°C. Cryostat frozen sectioned slices were incubated in TRAP staining solution for 1 hour at 37°C. For Alizarin Red staining, cells were fixed with 10% paraformaldehyde for 10 min before incubating in 1% Alizarin Red staining solution for 10 min, followed by washing three times. For ALP staining, cells and cryostat frozen sectioned slices were stained with a commercialized ALP kit (86R-1KT, MilliporeSigma) following the manufacturer's instructions. For SA-βGal staining, cells were fixed with 10% paraformaldehyde for 10 min before staining; both cells and cryostat frozen sectioned slices were stained with commercialized senescence cells histochemical staining kit (CS0030-1KT, MilliporeSigma) following manufacturer's instructions. For H&E

staining, paraffin-embedded slices were deparaffinized and stained with Hematoxylin Solution, Gill no. 2 (GHS216-500ML, MilliporeSigma), and Eosin Y Solution (HT110116-500ML, MilliporeSigma) following the manufacturer's instructions. All stained samples were scanned and imaged using an Eclipse Ti microscope (Nikon, Shinagawa, Japan).

Confocal microscopy
For cell imaging, all cells were fixed by 4% paraformaldehyde for 24 hours. After washing three times with PBS, cells were permeabilized with 0.3% Triton X-100 for 10 min and washed three times again with PBS. After blocking with PBS solution with 1% bovine serum albumin (BSA; B14, Thermo Fisher Scientific) for 1 hour, cells were incubated with indicated primary antibodies in PBS overnight at 4°C. The cells were then washed three times and incubated with accordant secondary antibodies in PBS containing 0.2% BSA for 2 hours at room temperature. After DAPI staining, cells were imaged by an A1R confocal microscope system (Nikon, Shinagawa, Japan). For bone slice imaging, 20-μm cryo-sectioned femur slices were prepared. Slices were permeabilized with 0.3% Triton X-100 for 10 min and washed three times with PBS. After blocking with PBS solution with normal donkey serum (566460, MilliporeSigma) for 1 hour, slices were incubated with indicated primary antibodies in PBS overnight at 4°C. The slices were then washed three times and incubated with accordant secondary antibodies in PBS containing 20% donkey serum for 2 hours at room temperature. After DAPI staining, each slice was imaged by A1R confocal microscope system (Nikon, Shinagawa, Japan). Antibodies and their working concentrations are listed in table S2.

Image quantification
For protein quantification in Western blot, ImageJ (version 1.52k; Bethesda, MD) was used to analyze the gray value of each band to represent intensity, which was normalized to β-actin or histone H3. For quantification of puncta area, ImageJ was applied to measure the area of puncta of different colors picked up by assigning "Hue" window in "color threshold" setting. The areas of fluorescence passing the color threshold in each image were recorded. For quantification of cell area, ImageJ was applied to measure the area of cells by assigning "brightness" window in color threshold setting. The areas of cells that pass the brightness threshold in each image were picked up and recorded. Each analysis was done three times to determine statistical significance.

Statistical analyses
Statistical analyses were performed using Prism 9 (GraphPad Software, San Diego, CA). Significance was determined as $P<0.05$. Comparisons with a specific control were assessed using Student's *t* test or one-way analysis of variance (ANOVA), followed by the Bonferroni's *t* test. Data are expressed as means ± SEM, Significance was shown as $*P<0.05$, $**P < 0.01$, or $***P < 0.001$.

Supplementary Materials
This PDF file includes:
Figs. S1 to S9
Tables S1 and S2

REFERENCES AND NOTES

1. S. He, N. E. Sharpless, Senescence in health and disease. *Cell* **169**, 1000–1011 (2017).

2. J. H. Morrison, P. R. Hof, Life and death of neurons in the aging brain. *Science* **278**, 412–419 (1997).

3. D. E. Bredesen, R. V. Rao, P. Mehlen, Cell death in the nervous system. *Nature* **443**, 796–802 (2006).

4. K. R. Chien, G. Karsenty, Longevity and lineages: Toward the integrative biology of degenerative diseases in heart, muscle, and bone. *Cell* **120**, 533–544 (2005).

5. T. Rezaie, A. Child, R. Hitchings, G. Brice, L. Miller, M. Coca-Prados, E. Heon, T. Krupin, R. Ritch, D. Kreutzer, R. P. Crick, M. Sarfarazi, Adult-onset primary open-angle glaucoma caused by mutations in optineurin. *Science* **295**, 1077–1079 (2002).

6. H. Maruyama, H. Morino, H. Ito, Y. Izumi, H. Kato, Y. Watanabe, Y. Kinoshita, M. Kamada, H. Nodera, H. Suzuki, O. Komure, S. Matsuura, K. Kobatake, N. Morimoto, K. Abe, N. Suzuki, M. Aoki, A. Kawata, T. Hirai, T. Kato, K. Ogasawara, A. Hirano, T. Takumi, H. Kusaka, K. Hagiwara, R. Kaji, H. Kawakami, Mutations of optineurin in amyotrophic lateral sclerosis. *Nature* **465**, 223–226 (2010).

7. O. M. Albagha, M. R. Visconti, N. Alonso, A. L. Langston, T. Cundy, R. Dargie, M. G. Dunlop, W. D. Fraser, M. J. Hooper, J. Isaia, G. C. Nicholson, R. del Pino Montes, R. Gonzalez-Sarmiento, M. di Stefano, A. Tenesa, J. P. Walsh, S. H. Ralston, Genome-wide association study identifies variants at CSF1, OPTN and TNFRSF11A as genetic risk factors for Paget's disease of bone. *Nat. Genet.* **42**, 520–524 (2010).

8. S. H. Ralston, A. L. Langston, I. R. Reid, Pathogenesis and management of Paget's disease of bone. *Lancet* **372**, 155–163 (2008).

9. F. R. Singer, Paget disease: When to treat and when not to treat. *Nat. Rev. Rheumatol.* **5**, 483–489 (2009).

10. G. A. Rodan, T. J. Martin, Therapeutic approaches to bone diseases. *Science* **289**, 1508–1514 (2000).

11. S. W. Wong, B. W. Huang, X. Hu, E. Ho Kim, J. P. Kolb, R. J. Padilla, P. Xue, L. Wang, T. H. Oguin III, P. A. Miguez, H. C. Tseng, C. C. Ko, J. Martinez, Global deletion of Optineurin results in altered type I IFN signaling and abnormal bone remodeling in a model of Paget's disease. *Cell Death Differ.* **27**, 71–84 (2020).

12. P. Xue, X. Hu, E. Chang, L. Wang, M. Chen, T. H. Wu, D. J. Lee, B. L. Foster, H. C. Tseng, C. C. Ko, Deficiency of optineurin enhances osteoclast differentiation by attenuating the NRF2-mediated antioxidant response. *Exp. Mol. Med.* **53**, 667–680 (2021).

13. W. Da, L. Tao, Y. Zhu, The role of osteoclast energy metabolism in the occurrence and development of osteoporosis. *Front. Endocrinol.* **12**, 675385 (2021).

14. D. B. Zorov, M. Juhaszova, S. J. Sollott, Mitochondrial reactive oxygen species (ROS) and ROS-induced ROS release. *Physiol. Rev.* **94**, 909–950 (2014).

15. T. S. Agidigbi, C. Kim, Reactive oxygen species in osteoclast differentiation and possible pharmaceutical targets of ROS-mediated osteoclast diseases. *Int. J. Mol. Sci.* **20**, (2019).

16. N. K. Lee, Y. G. Choi, J. Y. Baik, S. Y. Han, D. W. Jeong, Y. S. Bae, N. Kim, S. Y. Lee, A crucial role for reactive oxygen species in RANKL-induced osteoclast differentiation. *Blood* **106**, 852–859 (2005).

17. J. T. Coyle, P. Puttfarcken, Oxidative stress, glutamate, and neurodegenerative disorders. *Science* **262**, 689–695 (1993).

18. T. Tsunemi, T. D. Ashe, B. E. Morrison, K. R. Soriano, J. Au, R. A. Roque, E. R. Lazarowski, V. A. Damian, E. Masliah, A. R. La Spada, PGC-1α rescues Huntington's disease proteotoxicity by preventing oxidative stress and promoting TFEB function. *Sci. Transl. Med.* **4**, 142ra97 (2012).

19. F. Wauquier, L. Leotoing, V. Coxam, J. Guicheux, Y. Wittrant, Oxidative stress in bone remodelling and disease. *Trends Mol. Med.* **15**, 468–477 (2009).

20. Y. An, H. Zhang, C. Wang, F. Jiao, H. Xu, X. Wang, W. Luan, F. Ma, L. Ni, X. Tang, M. Liu, W. Guo, L. Yu, Activation of ROS/MAPKs/NF-κB/NLRP3 and inhibition of efferocytosis in osteoclast-mediated diabetic osteoporosis. *FASEB J.* **33**, 12515–12527 (2019).

21. M. Li, X. Xing, H. Huang, C. Liang, X. Gao, Q. Tang, X. Xu, J. Yang, L. Liao, W. Tian, BMSC-derived ApoEVs promote craniofacial bone repair via ROS/JNK signaling. *J. Dent. Res.* **101**, 714–723 (2022).

22. M. J. Morgan, Z. G. Liu, Crosstalk of reactive oxygen species and NF-κB signaling. *Cell Res.* **21**, 103–115 (2011).

23. Q. Ma, Role of nrf2 in oxidative stress and toxicity. *Annu. Rev. Pharmacol. Toxicol.* **53**, 401–426 (2013).

24. J. D. Hayes, M. McMahon, NRF2 and KEAP1 mutations: Permanent activation of an adaptive response in cancer. *Trends Biochem. Sci.* **34**, 176–188 (2009).

25. Q. Ma, X. He, Molecular basis of electrophilic and oxidative defense: Promises and perils of Nrf2. *Pharmacol. Rev.* **64**, 1055–1081 (2012).

26. J. M. Kim, C. Lin, Z. Stavre, M. B. Greenblatt, J. H. Shim, Osteoblast-osteoclast communication and bone homeostasis. *Cells* **9**, 2073 (2020).

27. H. Y. Ahn, K. E. Fairfull-Smith, B. J. Morrow, V. Lussini, B. Kim, M. V. Bondar, S. E. Bottle, K. D. Belfield, Two-photon fluorescence microscopy imaging of cellular oxidative stress using profluorescent nitroxides. *J. Am. Chem. Soc.* **134**, 4721–4730 (2012).

28. F. Debacq-Chainiaux, J. D. Erusalimsky, J. Campisi, O. Toussaint, Protocols to detect senescence-associated beta-galactosidase (SA-betagal) activity, a biomarker of senescent cells in culture and in vivo. *Nat. Protoc.* **4**, 1798–1806 (2009).

29. K. F. Azman, R. Zakaria, D-Galactose-induced accelerated aging model: An overview. *Biogerontology* **20**, 763–782 (2019).

30. S. Abrahams, W. L. Haylett, G. Johnson, J. A. Carr, S. Bardien, Antioxidant effects of curcumin in models of neurodegeneration, aging, oxidative and nitrosative stress: A review. *Neuroscience* **406**, 1–21 (2019).

31. S. H. Shahcheraghi, F. Salemi, N. Peirovi, J. Ayatollahi, W. Alam, H. Khan, L. Saso, Nrf2 regulation by curcumin: Molecular aspects for therapeutic prospects. *Molecules* **27**, 167 (2021).

32. R. Obaid, S. E. Wani, A. Azfer, T. Hurd, R. Jones, P. Cohen, S. H. Ralston, O. M. E. Albagha, Optineurin negatively regulates osteoclast differentiation by modulating NF-κB and interferon signaling: Implications for Paget's disease. *Cell Rep.* **13**, 1096–1102 (2015).

33. B. D'Autreaux, M. B. Toledano, ROS as signalling molecules: mechanisms that generate specificity in ROS homeostasis. *Nat. Rev. Mol. Cell Biol.* **8**, 813–824 (2007).

34. M. S. Cooke, M. D. Evans, M. Dizdaroglu, J. Lunec, Oxidative DNA damage: Mechanisms, mutation, and disease. *FASEB J.* **17**, 1195–1214 (2003).

35. N. M. Khan, A. Haseeb, M. Y. Ansari, P. Devarapalli, S. Haynie, T. M. Haqqi, Wogonin, a plant derived small molecule, exerts potent anti-inflammatory and chondroprotective effects through the activation of ROS/ERK/Nrf2 signaling pathways in human osteoarthritis chondrocytes. *Free Radic. Biol. Med.* **106**, 288–301 (2017).

36. Y. Liu, C. Wang, G. Wang, Y. Sun, Z. Deng, L. Chen, K. Chen, J. Tickner, J. Kenny, D. Song, Q. Zhang, H. Wang, Z. Chen, C. Zhou, W. He, J. Xu, Loureirin B suppresses RANKL-induced osteoclastogenesis and ovariectomized osteoporosis via attenuating NFATc1 and ROS activities. *Theranostics* **9**, 4648–4662 (2019).

37. M. Arra, G. Swarnkar, K. Ke, J. E. Otero, J. Ying, X. Duan, T. Maruyama, M. F. Rai, R. J. O'Keefe, G. Mbalaviele, J. Shen, Y. Abu-Amer, LDHA-mediated ROS generation in chondrocytes is a potential therapeutic target for osteoarthritis. *Nat. Commun.* **11**, 3427 (2020).

38. X. Sun, Z. Xie, B. Hu, B. Zhang, Y. Ma, X. Pan, H. Huang, J. Wang, X. Zhao, Z. Jie, P. Shi, Z. Chen, The Nrf2 activator RTA-408 attenuates osteoclastogenesis by inhibiting STING dependent NF-κb signaling. *Redox Biol.* **28**, 101309 (2020).

39. L. Xiao, M. Zhong, Y. Huang, J. Zhu, W. Tang, D. Li, J. Shi, A. Lu, Y. Yang, D. Geng, H. Li, Z. Wang, Puerarin alleviates osteoporosis in the ovariectomy-induced mice by suppressing osteoclastogenesis via inhibition of TRAF6/ROS-dependent MAPK/NF-κB signaling pathways. *Aging* **12**, 21706–21729 (2020).

40. J. Gao, M. Ohtsubo, Y. Hotta, S. Minoshima, Oligomerization of optineurin and its oxidative stress- or E50K mutation-driven covalent cross-linking: Possible relationship with glaucoma pathology. *PLOS ONE* **9**, e101206 (2014).

41. M. Zhu, A. Li, J. Chen, S. Zhang, J. Wu, Effects of optineurin mutants on SH-SY5Y cell survival. *Mol. Cell. Neurosci.* **74**, 18–24 (2016).

42. T. K. Basu, M. Smethurst, M. B. Gillett, D. Donaldson, S. J. Jordan, D. C. Williams, J. A. Hicklin, Ascorbic acid therapy for the relief of bone pain in Paget's disease. *Acta Vitaminol. Enzymol.* **32**, 45–49 (1978).

43. M. Smethurst, T. K. Basu, M. B. Gillett, D. Donaldson, S. J. Jordan, D. C. Williams, J. A. Hicklin, Combined therapy with ascorbic acid and calcitonin for the relief of bone pain in Paget's disease. *Acta Vitaminol. Enzymol.* **3**, 8–11 (1981).

44. S. C. Manolagas, From estrogen-centric to aging and oxidative stress: A revised perspective of the pathogenesis of osteoporosis. *Endocr. Rev.* **31**, 266–300 (2010).

45. J. N. Farr, M. Xu, M. M. Weivoda, D. G. Monroe, D. G. Fraser, J. L. Onken, B. A. Negley, J. G. Sfeir, M. B. Ogrodnik, C. M. Hachfeld, N. K. LeBrasseur, M. T. Drake, R. J. Pignolo, T. Pirtskhalava, T. Tchkonia, M. J. Oursler, J. L. Kirkland, S. Khosla, Targeting cellular senescence prevents age-related bone loss in mice. *Nat. Med.* **23**, 1072–1079 (2017).

46. X. Li, Y. Chen, Y. Mao, P. Dai, X. Sun, X. Zhang, H. Cheng, Y. Wang, I. Banda, G. Wu, J. Ma, S. Huang, T. Forouzanfar, Curcumin protects osteoblasts from oxidative stress-induced dysfunction via GSK3β-Nrf2 signaling pathway. *Front. Bioeng. Biotechnol.* **8**, 625 (2020).

47. H. E. Son, E. J. Kim, W. G. Jang, Curcumin induces osteoblast differentiation through mild-endoplasmic reticulum stress-mediated such as BMP2 on osteoblast cells. *Life Sci.* **193**, 34–39 (2018).

48. Y. Zhou, Y. Deng, Z. Liu, M. Yin, M. Hou, Z. Zhao, X. Zhou, L. Yin, Cytokine-scavenging nanodecoys reconstruct osteoclast/osteoblast balance toward the treatment of post-menopausal osteoporosis. *Sci. Adv.* **7**, eabl6432 (2021).

49. T. Hortobagyi, C. Troakes, A. L. Nishimura, C. Vance, J. C. van Swieten, H. Seelaar, A. King, S. Al-Sarraj, B. Rogelj, C. E. Shaw, Optineurin inclusions occur in a minority of TDP-43 positive ALS and FTLD-TDP cases and are rarely observed in other neurodegenerative disorders. *Acta Neuropathol.* **121**, 519–527 (2011).

50. L. Liu, K. Zhang, H. Sandoval, S. Yamamoto, M. Jaiswal, E. Sanz, Z. Li, J. Hui, B. H. Graham, A. Quintana, H. J. Bellen, Glial lipid droplets and ROS induced by mitochondrial defects promote neurodegeneration. *Cell* **160**, 177–190 (2015).

51. E. Tonnies, E. Trushina, Oxidative stress, synaptic dysfunction, and Alzheimer's disease. *J. Alzheimers Dis.* **57**, 1105–1121 (2017).

52. A. Singh, R. Kukreti, L. Saso, S. Kukreti, Oxidative stress: A key modulator in neurodegenerative diseases. *Molecules* **24**, (2019).

53. L. Wang, T.-H. Wu, X. Hu, J. Liu, D. Wu, P. A. Miguez, J. T. Wright, S. Zhang, J.-T. Chi, H. C. Tseng, C. C. Ko, Biomimetic polydopamine-laced hydroxyapatite collagen material orients osteoclast behavior to an anti-resorptive pattern without compromising osteoclasts' coupling to osteoblasts. *Biomater. Sci.* **9**, 7565–7574 (2021).